

The Journal of Physiology

<https://jp.msubmit.net>

JP-RP-2023-285490R2

Title: Role of Tissue Biomechanics in the Formation and Function of Myocardial Trabeculae in Zebrafish Embryos

Authors: Adriana Gaia Cairelli
Alex Gendernalik
Wei Xuan Chan
Phuc Nguyen
Julien Vermot
Juhyun Lee
David Bark
Choon Hwai Yap

Author Conflict: No competing interests declared

Author Contribution: Adriana Gaia Cairelli: Conception or design of the work; Acquisition, analysis or interpretation of data for the work; Drafting the work or revising it critically for important intellectual content; Final approval of the version to be published; Agreement to be accountable for all aspects of the work Alex Gendernalik: Acquisition, analysis or interpretation of data for the work; Drafting the work or revising it critically for important intellectual content; Final approval of the version to be published; Agreement to be accountable for all aspects of the work Wei Xuan Chan: Acquisition, analysis or interpretation of data for the work;

Disclaimer: This is a confidential document.

Drafting the work or revising it critically for important intellectual content; Final approval of the version to be published; Agreement to be accountable for all aspects of the work Phuc Nguyen: Acquisition, analysis or interpretation of data for the work; Drafting the work or revising it critically for important intellectual content; Final approval of the version to be published; Agreement to be accountable for all aspects of the work Julien Vermot: Conception or design of the work; Drafting the work or revising it critically for important intellectual content; Final approval of the version to be published; Agreement to be accountable for all aspects of the work Juhyun Lee: Acquisition, analysis or interpretation of data for the work; Drafting the work or revising it critically for important intellectual content; Final approval of the version to be published; Agreement to be accountable for all aspects of the work David Bark: Conception or design of the work; Acquisition, analysis or interpretation of data for the work; Drafting the work or revising it critically for important intellectual content; Final approval of the version to be published; Agreement to be accountable for all aspects of the work Choon Hwai Yap: Conception or design of the work; Acquisition, analysis or interpretation of data for the work; Drafting the work or revising it critically for important intellectual content; Final approval of the version to be published; Agreement to be accountable for all aspects of the work

Running Title: Biomechanics in Formation and Function of Embryonic Heart Trabeculae

Dual Publication: No

Funding: Imperial College London (ICL): Choon Hwai Yap, startup funding

1 **Role of Tissue Biomechanics in the Formation and Function of**
2 **Myocardial Trabeculae in Zebrafish Embryos**

3

4 **Adriana Gaia Cairelli¹, Alex Gendernalik², Wei Xuan Chan¹, Phuc Nguyen³,**
5 **Julien Vermot¹, Juhyun Lee³, David Bark Jr.², Choon Hwai Yap*¹**

6 ¹ *Dept of Bioengineering, Imperial College London, London, United Kingdom*

7 ² *Department of Pediatrics, Washington University in St. Louis, St. Louis, United*
8 *States of America*

9 ³ *Department of Bioengineering, University of Texas at Arlington, Arlington, United*
10 *States of America*

11

12

13

14 Corresponding author:

15 Choon Hwai Yap

16 Senior Lecturer,

17 Dept. of Bioengineering,

18 Imperial College London, London, UK.

19 (e-mail: c.yap@imperial.ac.uk)

20

21 **Keywords:** Embryonic Heart, Cardiac Tabeculation, Computational Biomechanics,
22 Trabeculation Formation and Function. Myocardial Strains and Stresses.

23 **Running Title:** Biomechanics in Formation and Function of Embryonic Heart
24 Trabeculae

25 **Key Points**

- 26 • Trabeculations are fascinating and important cardiac structures, their
27 abnormalities are linked to embryonic demise.
- 28 • However, their function in the heart and their mechanobiological formation
29 processes are not completely understood.
- 30 • Our imaging and modelling show that tissue biomechanics is the key here.
31 We find that trabeculations enhance cardiac wall deformability, reduce fluid
32 pressure stresses, homogenize wall stiffness, and have alignments that are
33 optimal for providing load-bearing structural support for the heart.
- 34 • We further discover that high ventricular tissue internal stresses consequent
35 to high fluid pressures are needed for trabeculation formation through a
36 rescue experiment, demonstrating that myocardial tissue stresses are as
37 important as fluid flow wall shear stresses for trabeculation formation.

38 **Abstract**

39 Cardiac trabeculae are uneven ventricular muscular structures that develop
40 during early embryonic heart development at the outer curvature of the ventricle.
41 However, their biomechanical function is not completely understood, and while their
42 formation is known to be mechanosensitive, it is unclear if ventricular tissue internal
43 stresses play an important role in their formation. Here, we performed imaging and
44 image-based cardiac biomechanics simulations on zebrafish embryonic ventricles to
45 investigate these issues. Microscopy-based ventricular strain measurements show
46 that the appearance of trabeculae coincided with enhanced deformability of the
47 ventricular wall. Image-based biomechanical simulations reveal that the presence of
48 trabeculae reduces ventricular tissue internal stresses, likely acting as structural

49 support in response to the geometry of the ventricle. Passive ventricular pressure
50 loading experiments further reveal that the formation of trabeculae is associated with
51 a spatial homogenization of ventricular tissue stiffnesses in healthy hearts, but gata1
52 morphants with a disrupted trabeculation process retain a spatial stiffness
53 heterogeneity. Our findings thus suggest that modulating ventricular wall
54 deformability, stresses, and stiffness are among the biomechanical functions of
55 trabeculae. Further, experiments with gata1 morphants reveal that a reduction in
56 fluid pressures and consequently ventricular tissue internal stresses can disrupt
57 trabeculation, but a subsequent restoration of ventricular tissue internal stresses via
58 vasopressin rescues trabeculation, demonstrating that tissue stresses are important
59 to trabeculae formation. Overall, we find that tissue biomechanics are important to
60 the formation and function of embryonic heart trabeculation.

61

62 **Introduction**

63 In the process of development of the ventricle, the myocardium differentiates
64 into two layers, a compact and a trabeculated zone, both of which are likely essential
65 for normal cardiac contractile function. The trabeculae are myocardial cells covered
66 by an endocardial layer, that form a complex network of contractile bundles
67 crisscrossing the inner surface of the ventricle. Interestingly, they only form on the
68 outer curvature of the ventricle, opposite to the atrioventricular canal. The trabeculae
69 appear to function as a rapid conduction system in cardiac electrophysiology
70 (Srivastava & Olson, 2000) and are hypothesised to improve nutrition transport to the
71 heart, before the development of the coronary arteries, by increasing the surface
72 area available for biotransport (Samsa *et al.*, 2013). Many mutants with defects in

73 trabeculations or the suppression of genes involved in trabeculation formation, end
74 with embryonic mortality (Gassmann *et al.*, 1995; Lai *et al.*, 2010; Liu *et al.*, 2010),
75 suggesting that they may be essential for life. However, whether and how the
76 trabeculae contribute to the pumping function of the heart is not completely
77 understood and is investigated here.

78 Previous research has demonstrated that ventricular chamber maturation and
79 trabeculae formation are mechanosensitive processes (Hove *et al.*, 2003; Miller,
80 2011; Duchemin *et al.*, 2019), such that when the biomechanical environment is
81 disrupted, defective heart morphogenesis and abnormalities occur (Staudt *et al.*,
82 2014; Lee *et al.*, 2016; Rasouli & Stainier, 2017; Foo *et al.*, 2021). Many past authors
83 have attributed trabeculae formation to stimuli provided by fluid shear stresses
84 imposed on endothelial surface (or fluid wall shear stresses, WSS) (Hove *et al.*,
85 2003; Granados-Riveron & Brook, 2012; Boselli *et al.*, 2015; Vedula *et al.*, 2017; Lee
86 *et al.*, 2018; Cavallero *et al.*, 2021; Foo *et al.*, 2021), as biomechanical disruption
87 involving reduction of cardiac flow prevented trabeculation. However, on top of
88 reducing fluid WSS, these disruptions likely caused a reduction in chamber fluid
89 pressure and consequently ventricular tissue internal stresses as well (or tissue
90 stresses, defined as stresses imposed by neighbouring pieces of ventricular wall
91 tissues on one another). It is unclear if tissue internal stresses played an important
92 role as well. In our previous microscopy-based flow simulations (Cairelli *et al.*, 2022),
93 we found that there were widely varying fluid WSS characteristics at regions that
94 trabeculated, and the general fluid WSS characteristics at regions that trabeculated
95 did not differ from regions that did not. This suggested that fluid WSS may not be the
96 only stimuli needed for trabeculation. We speculate that ventricular tissue internal

97 stresses are a second stimuli important for this process, and we investigate this
98 here.

99 In the current study, we firstly investigate if and how embryonic cardiac
100 trabeculation confer biomechanical advantages to the function of the heart, and
101 secondly test the hypothesis that ventricular tissue internal stresses play a role in
102 trabeculation formation, using a combination of microscopy imaging of zebrafish
103 embryonic hearts, image processing, cardiac finite element modelling and
104 experimental data.

105 **Results**

106 ***Trabeculae enhance deformability of myocardial walls***

107 To determine if the presence of trabeculae alters the deformational behaviour
108 of the embryonic heart walls, we first perform high-resolution 4D lightsheet
109 microscopy imaging of the zebrafish embryonic heart with myocardial tags, using the
110 *Tg(cmhc2:GFP)* zebrafish transgenic line, between 2 and 3 dpf, before and after
111 trabeculation. We performed segmentation and motion tracking of the embryonic
112 heart from images, using a validated cardiac motion estimation algorithm (Wiputra et
113 al., 2020), and calculated 3D strains of myocardial walls using previous methods
114 (Zheng et al., 2022; Ren et al., 2023). Supplementary Video 1 and Figure 1A show
115 that satisfactory segmentation and high-fidelity motion tracking are performed.

116 Myocardial strain analysis (MSA) results for the zebrafish embryonic ventricle
117 are shown in Figure 1. The computed strains are between the end-diastolic and end-
118 systolic time steps, with end-diastole as the zero reference, and are averaged
119 spatially for specific zones. Strain components are quantified in the direction of the

120 lowest eigenvector of the strain tensor, which represents the direction of maximum
121 contraction and is likely close to the myocyte direction.

122 Results in Figure 1C showed that before and after trabeculation, the
123 deformational characteristics change. In the pre-trabeculated ventricles, fiber
124 direction strain at the inner curvature region is significantly higher than the one at the
125 outer curvature region. In contrast, in the trabeculated ventricles, the opposite
126 occurs, with the outer curvature region showing significantly higher fiber direction
127 strain than inner curvature region. This suggests that the emergence of the
128 trabeculation at the outer curvature region enhances wall strains at that region.

129 To understand this further, we focused on individual trabeculae and
130 performed more detailed motion tracking and strain calculations (Figure 1D-E).
131 Results show that trabeculation bundles underwent significantly higher fiber direction
132 contractile strains than their surrounding compact myocardial tissues, for all
133 developmental stages investigated. The 3D reconstruction of the contractile motion
134 of a typical trabecula and its surrounding compact myocardial tissue is demonstrated
135 by Supplementary Video 2, which clearly demonstrated the trabecula exhibiting
136 higher strain along its alignment direction than surrounding myocardial tissues. We
137 speculate that this could be due to trabeculae having stronger contractile forces, or
138 due to trabeculae experiencing reduced constraints from surrounding tissues, since
139 they are structures protruding from the cardiac wall and have reduced surrounding
140 tissue to constrain their motion. Myocardial tissues are composed mostly of water, so
141 they are likely near to being incompressible, and as such, they need to expand
142 laterally during contraction. Having reduced surrounding tissues thus facilitates
143 contractile deformations.

144 Taken together, our imaging and motion tracking show that the emergence of
145 trabeculation enhanced contractile deformations of the cardiac wall, and that
146 trabeculae exhibited stronger contractile deformations than surrounding tissues.
147 Cardiac trabeculae could thus function to enhance contractile deformation.

148 ***Formation of trabeculae coincide with high myocardial tissue internal stresses***

149 Our 4D light-sheet microscopy images show visual geometrical changes
150 across developmental stages at the outer curvature zones that suggest cardiac wall
151 stresses are likely to change during the timing when trabeculation forms between 2
152 and 3 dpf. We assess these geometric changes and perform FE simulations to
153 assess tissue stresses, as shown in Figure 2.

154 We assessed the circumferential geodesic curvature of the ventricle by
155 extracting 3 cross-sections at the middle 60% of the ventricle at end-systole,
156 obtaining the mid-wall line (in between endo- and epicardial surfaces) of the
157 myocardium on each cross-section, calculating the geodesic curvature of this mid-
158 wall line, and spatially averaging geodesic curvatures for the outer curvature zone,
159 as shown in Figure 2A-B. Results in Figure 2C show that there is a substantial
160 increase in the circumferential geodesic curvature at the outer curvature zone from 2
161 dpf to 3 dpf, from before to after trabeculation, suggesting that the heart becomes
162 more elliptical. In an elliptical pressure vessel, stresses tend to concentrate at the
163 edge with sharper curvature (Utagikar & Naik, 2013), which corresponds to the outer
164 curvature zone.

165 Further, myocardial wall thicknesses are evaluated from the 3D reconstruction
166 at end-systole at the outer curvature region (indicated by the box in Figure 2D) and
167 spatially averaged. Results show that the outer curvature region becomes thinner

168 from 2 to 3 dpf (Figure 2D-E), continue to become thinner at 4 dpf before thickening
169 again at 5 dpf. The reduction in thickness from 2 to 3 dpf occurs during trabeculation
170 formation, and although trabeculations increases the thickness locally where they
171 are formed, majority of the myocardial wall is composed of compact layer only after
172 trabeculation, and these locations experience thinning over the trabeculation
173 development process.

174 Our geometric characterization thus suggests that stresses likely increases in
175 the outer curvature zone mainly due to a decrease in wall thickness of the outer
176 curvature zone, coupled with an increase in cavity pressure with age (Salehin *et al.*,
177 2021). The ventricle also adopted a more elliptical shape, which is likely to contribute
178 further to the increased tissue stress at this zone.

179 To assess ventricular tissue internal stresses, we performed subject-specific
180 microscopy image-based finite-element (FE) simulations, using a model that is
181 previously used to model adult and fetal cardiac biomechanics (Ong *et al.*, 2021).
182 Here, the 3D reconstruction of the ventricle is used for simulations of its contraction
183 biomechanics as explained in the methods section. A transversely isotropic
184 hyperelastic passive stiffness model (where stiffness is higher in the myofiber
185 direction than other directions) and the Guccione active tension generation were
186 specified in the simulations. The spatially varying direction of tension generation is
187 specified as the minimum eigenvector of the 3D strain tensor from motion tracking of
188 microscopy images, as this represents the direction of the greatest shortening and is
189 the likely direction of force generation. A lumped-parameter model is coupled to the
190 FE model to enable realistic pressure and flow rate calculations.

191 FE simulated ventricular tissue stress results are shown in Figure 2F-G.
192 Results show that, from 2 to 3 dpf, as the outer curvature region becomes thinner
193 and more curved, there is an accumulation of tissue stress magnitude (quantified as
194 the L2 norm of the stress tensor) in this region (Figure 2F). The spatial average of
195 tissue stress magnitude is shown in Figure 2G, demonstrating that at 2 dpf, the outer
196 curvature region experiences lower stresses than the inner curvature zone, but at 3
197 dpf, this trend is reversed, and the outer curvature region starts experiencing higher
198 stresses. Myocardial strains from our FE simulations corroborates observations from
199 image motion tracking discussed above, where the outer curvature region
200 experiences increased fiber direction strains from 2 to 3 dpf, and while it is initially
201 lower than strains at the inner curvature zone at 2 dpf, it become higher at 3 dpf
202 (Figure 2H).

203 Taken together, our data suggest that changes to cardiac wall geometry and
204 tissue internal stresses occur around the time that trabeculation develops from 2 to 3
205 dpf, which, as our simulations show, leads to concentration of stresses at the outer
206 curvature region. We hypothesize that the trabeculae are formed to reduce this
207 tissue stress burden.

208 ***Trabeculae reduce the overall myocardial tissue stress burden***

209 The 3dpf zebrafish embryonic heart is more curved circumferentially than
210 longitudinally (Figure 3A). To understand whether tissue stresses in the ventricular
211 walls are aligned in the circumferential or the longitudinal direction, we performed
212 image-based FE simulations of the 3 dpf ventricle during the diastolic passive
213 pressure loading phase. We find that the consequent ventricular tissue stresses are
214 higher in the circumferential direction than in the longitudinal direction (Figure

215 3CFigure and Figure 3I). Interestingly, stresses in the two directions are
216 approximately equal at 2dpf, suggesting as the ventricle become more elliptical with
217 growth, directionality of stress develops.

218 In the 3dpf ventricle, Figure given the typically circumferential direction of the
219 trabeculae, they are ideal structures to provide bracing for the cardiac walls to
220 counter elevated circumferential stresses. We performed further FE simulations to
221 investigate if a circumferential alignment of myofibers can reduce myocardial tissue
222 stresses, to infer if the circumferential alignment of trabeculation can reduce stresses
223 as well. We performed simulations on the same ventricles, imposing a fully
224 circumferential alignment of myofibers, and then a full longitudinal alignment of the
225 myofibers. Ventricular tissue stress results in Figure 3B show that a circumferential
226 alignment of the myofibers allow a reduction of tissue stress in all directions (around
227 1.5 times for the circumferential stress and around 2 times for the longitudinal stress)
228 compared to a longitudinal alignment. This shows that by aligning stress bearing
229 structures and contractile forces in the direction of highest passive stress, the overall
230 myocardial tissue stress can be reduced. As such, by aligning the trabeculae
231 circumferentially, they are in the best alignment to counter high circumferential
232 stresses of the ventricular walls as load-bearing structures and contractile apparatus,
233 to reduce overall myocardial tissue stresses.

234 To demonstrate that cardiac trabeculae act as structure bridges at high tissue
235 stress locations to reduce stresses, we reperform FE simulations of 3 dpf embryonic
236 hearts after smoothing out trabeculae features on the inner surface, to compare with
237 original FE simulations with intact trabeculae, while maintaining the same myocardial
238 mass for both simulations. FE simulations are run by coupling them to simplified

239 lumped-parameter models (as shown in Figure 7 in methods section), using the
240 same parameters for simulations with and without trabeculae. Parameter values are
241 given in Table 2.

242 Figure 3D shows a typical model before and after removing trabeculae. Figure
243 3E shows the simulation results, demonstrating the presence of high myocardial
244 tissue stresses (L2 norm of the stress tensor) at the outer curvature region,
245 highlighted with the box outline, and demonstrating that in the trabeculated model,
246 high stresses regions are broken up by regions of lower stress. Figure 3F-G show
247 the pressure-volume (P-V) loops from the simulations, as well as stress magnitudes,
248 spatially averaged over the ventricle, over a cardiac cycle. In these simulations, the
249 use of a lumped parameter model allows modelling of ventricular-vascular coupling.
250 From this, we observed a P-V loop (Figure 3F) that has substantial similarity with
251 previous experimental measurements (Salehin *et al.*, 2021), although there are
252 minor features, such as a transient negative pressure during early diastole that was
253 not captured by our simulation. Results in Figure 3G shows that the trabeculated
254 model has lower ventricular tissue stresses than the smooth model at peak systole.
255 In Figure 3G, statistical testing shows that the ratio of peak systolic stress in smooth
256 versus trabeculated models is significantly greater than one.

257 To ensure that our simulation conclusions are robust, we further perform
258 simulations where the volume of the ventricle is prescribed by the volume measured
259 from microscopy images across the cardiac cycle, instead of calculated via the
260 lumped-parameter model (Figure 7Figure). We similarly observed that stresses are
261 higher in the myocardium of the smooth model compared to the trabeculated model,
262 whether or not we adjusted to contractility to match the peak systolic pressure of the

263 two models. This demonstrates that trabeculae reduce ventricular tissue stresses
264 and can do so without sacrificing stroke volume and pressure generation cardiac
265 functions.

266 Taken together, our results support our hypothesis that trabeculae
267 morphology is optimized for structural support and to reduce the stresses of the
268 ventricular tissues at the outer curvature region of the ventricle, to counter a
269 concentration of high stress there.

270 **High cardiac wall stress rescues disrupted trabeculation formation in Gata1**
271 **morpholino treated zebrafish embryonic hearts**

272 To investigate the hypothesis that cardiac tissue stresses are important stimuli
273 for trabeculation formation, we study *gata1 morphant* zebrafish embryos, which
274 feature disrupted trabecular development (Galloway *et al.*, 2005). In this model,
275 injected morpholino oligos are used to inhibit the formation of red blood cells,
276 resulting in a blood composition of almost entirely plasma. This is likely to reduce
277 blood viscosity by 4.9 times, as previous experimental measurements approximated
278 zebrafish whole blood viscosity to be 7.35cP (Lee *et al.*, 2017) while the
279 corresponding blood plasma viscosity to be 1.5cP, and thus the pressure required for
280 cardiac fluid pumping will be similarly reduced. The reduction in ventricular pressure
281 will subsequently reduce distention of the ventricle and reduce ventricular tissue
282 tensile stresses. Previous investigators also anticipated that the lack of blood
283 particles in blood will decrease fluid wall shear stresses imposed on the endocardial
284 surface (Vedula *et al.*, 2017; Lee *et al.*, 2018). Likely consequent to these
285 biomechanical disruptions, the *gata1 morphants* develop a ventricular surface that is

286 much smoother than the wild-type zebrafish, with drastically reduced trabecular
287 structures (Vedula *et al.*, 2017; Lee *et al.*, 2018).

288 To test if increased ventricular tissue stresses can rescue trabeculation
289 formation, *gata1 morphants* were treated with vasopressin, a potent vasoconstrictor
290 (Ahuja *et al.*, 2022) for 3 days starting at 1 dpf until 4 dpf. Previous measurements
291 show that this treatment reduces zebrafish embryonic vascular dimensions, which
292 should lead to elevated peripheral blood flow resistance and cardiac afterload,
293 without reducing cardiac output (Ahuja *et al.*, 2022). This will increase the pressures
294 needed to drive circulation, elevate cardiac pressures, leading to increased
295 distention of the ventricle, and thus increase ventricular tissue stresses.

296 At 4 dpf, the trabeculation morphology for the *gata1 morphants*, vasopressin-
297 treated *gata1 morphants*, and non-morphant controls, which are all generated from
298 the myocardial tagged line *Tg(cmlc2:GFP)*, are investigated via 3D confocal
299 microscopy. Results in Figure 4A show that *gata1 morphants* have myocardium that
300 is significantly smoother on the inner surfaces, but with the vasopressin treatment,
301 the myocardium restored its complex undulating inner surface. The amount of
302 trabecular layer tissue is estimated by manual segmentation of the entire
303 myocardium as well as just the compact myocardium (Figure 4B), followed by 3D
304 reconstruction and volume estimation as previously described (Lee *et al.*, 2016). The
305 quantification of volume of trabeculation tissue is done by subtraction of the two
306 abovementioned volumes. Results in Figure 4C shows a significantly reduced
307 trabecular layer tissue volume in *gata1 morphants*, but with vasopressin, the amount
308 of trabecular layer tissue volume restores close to controls and is significantly
309 different from *gata1 morphants*.

310 To validate that intraventricular pressures were altered in *gata1 morphants*
311 and with *vasopressin* treatment, we performed direct pressure measurements using
312 a servo-null system as previously described (Salehin *et al.*, 2021). Results in Figure
313 4D confirms that *gata1 morphants* exhibit significantly lower peak ventricular
314 pressures compared to healthy control embryonic hearts, the addition of *vasopressin*
315 significantly increased peak ventricular pressures from *gata1 morphants*. To confirm
316 that lower pressure in *gata1 morphants* is also leading lower myocardial tissue
317 stresses, additional FE simulations were performed. In this case, the Windkessel
318 resistances were scaled based on the ratio in peak pressure between controls and
319 *gata1 morphants* (a 1.6x difference) with minor tuning to adjust the shape of the PV
320 loop. The analogous was done between controls and *gata1 morphants* with
321 *vasopressin* treatment, scaling by a 1.2x ratio of pressures. The results in Figure
322 4E-F confirmed that myocardial tissue stresses are reduced in *gata1 morphants*
323 compared to controls, consequent to the lower ventricular blood pressures.

324 Taken together, our data show that tissue stresses in the ventricular wall are
325 important stimuli for trabeculation formation, given that reduced stresses in *gata1*
326 *morphants* prevented the formation, and the subsequently increased tissue stresses
327 via *vasopressin* treatment rescued the formation, and given that fluid wall shear
328 stresses cannot account for these observations.

329 **Trabeculation formation leads to spatial homogenization of ventricular wall
330 stiffnesses**

331 Given the stress-driven nature of the formation of the trabeculae and the
332 trabeculae's ability to enhance the tissue deformability and reduce tissue stress, we
333 investigate if their presence influences the overall stiffness of the myocardial wall. To

334 do this, we perform passive pressurizations of zebrafish embryonic hearts paired
335 with subject-specific image-based FE modelling of the pressurization process, to
336 determine the spatial variation of tissue stiffness.

337 Passive pressurization is achieved by stopping the heartbeat with BDM and
338 pushing fluid into the embryonic atria via a micropipette equipped with pressure
339 control, as previously described (Gendernalik *et al.*, 2021). 3D microscopy imaging
340 and pressure measurements are concurrently performed during the pressurization
341 and are later used in the FE modelling of the pressurization process. The same
342 images from the pressurization experiments are used to estimate actual myocardial
343 strains using the MSA technique described above. In the FE simulations, pressure-
344 induced stretch with no active tension is modelled, using the assumption of a
345 spatially uniform passive stiffness material property. Comparing longitudinal-
346 circumferential areal stretch deformations from the FE results and image MSA,
347 regions where MSA stretch are lower than the FE stretch are where the stiffness are
348 underestimated in the simulations, while regions with MSA stretch are higher than
349 the FE stretch are regions where stiffness are overestimated in the simulation. This
350 thus enables an evaluation of the spatial variability of tissue stiffness.

351 Results of this analysis are presented in Figure 5, Figure and Table 1. The
352 healthy control ventricles at 2dpf, before trabeculation, consistently demonstrated
353 clear bands of stiffness inhomogeneity, while in control ventricles at 3dpf, these
354 bands can no longer be clearly observed, suggesting a spatial stiffness
355 homogeneity. Interestingly, in the *gata1* morphants at 3dpf, where trabeculations
356 formation is disrupted, substantial spatial inhomogeneity and bands of stiffness
357 differences can still be observed in 2 out of 3 samples examined. The results thus
358 suggest that the formation of the trabeculations causes a spatial homogeneity of

359 ventricular wall stiffness, while a disruption of the trabeculations formation process
360 prevents this homogeneity. We thus speculate that a further function of the cardiac
361 trabeculae is to achieve a spatial homogeneity of biomechanical behaviours.

362 **Discussion**

363 In the current study, we find that ventricular tissue biomechanics is in fact an
364 important aspect of embryonic heart trabeculation function and an important stimulus
365 for trabeculation formation. Our results suggest three functions for trabeculations.
366 First, they enhance tissue deformability to facilitate cardiac pumping actions, second,
367 they counter high myocardial tissue stresses with active tension and reduce
368 myocardial tissue stresses as structural support, and third, they reduce spatial
369 inhomogeneity of tissue stiffness.

370 Our strain measurement results agreed well with the literature. Our
371 observation that the embryonic heart deforms more in the circumferential direction
372 than in the longitudinal direction corroborated with observations of the same in a
373 recent earlier study by Salehin et al (Salehin et al., 2022). Further, in both our strain
374 measurements from image tracking (Figure 1C) and strain results from FE
375 simulations (Figure 2H), the outer curvature region of the ventricle is more
376 deformable after trabeculae formation. Our results corroborated a previous study by
377 Teranikar et al. on myocardial areal stretch obtained from tracking of cardiomyocyte
378 nuclei (Teranikar, 2021), which similarly found that the areal stretch of the outer
379 curvature region is higher than that of the inner curvature region, and which found
380 that the observation is consistently observed across developmental stages between
381 2-5 dpf, and despite increasing contractility with age (Teranikar, 2021). A further
382 recent study by Priya et al. on the initial phases of trabeculation formation showed

383 that cardiomyocytes with greater contractility delaminate from the compact layer and
384 seed the trabecular layer, while less contractile ones stay in the compact layer (Priya
385 *et al.*, 2020). This suggests that trabecular myocytes will be more contractile and
386 corroborates with our observation that trabecular bundles undergo greater contractile
387 strains than their surrounding compact myocardium (Figure 1E).

388 In our strain measurements, we observed enhanced deformability of the
389 trabeculate zone in both the longitudinal and circumferential directions. In the
390 circumferential direction, this enhancement is likely due to the ability of trabeculae
391 bundles to undergo larger contractions than the surrounding compact layer (Figure
392 1E), as most trabeculae bundles are aligned circumferentially. As for the enhanced
393 strain in the longitudinal direction, this is likely unrelated to contractile forces, but due
394 to the thinning of the compact layer at the trabeculated regions and the consequently
395 reduced passive stiffness of the corrugated surface structure after trabeculation
396 formation, which thus enables larger longitudinal stretch in these trabeculated
397 regions.

398 Our results further suggest that between 2 and 3dpf, during trabeculation
399 formation, there are thickness changes to the outer curvature of the ventricle and an
400 overall change of ventricular shape to be elliptical, that leads to stress concentration
401 in the outer curvature region, and that cardiac trabeculae formation can mitigate the
402 high stresses, suggesting this mitigation as one of their functions. Our simulations
403 also show that the circumferential orientation of the trabeculae has useful effects of
404 countering high circumferential stresses and have an overall stress reduction effect
405 in the myocardium. The morphology of the trabeculae is akin to that of a linear
406 bracing beam bridging across a curved structural surface, the compact myocardium,

407 to support the curved surface, which is a common structural engineering strategy.
408 This can explain the wall stress differences between the trabeculated and smooth
409 FE models (Figure 2F-G), and makes it logical to assume that the trabeculae have
410 structural load bearing roles. Our results in Figure 3B corroborated this notion, by
411 showing that the typically circumferential alignment of structural fibres can lead to
412 reduction of overall myocardial stresses, consequent to the geometry of the heart,
413 which is more curved circumferentially than longitudinally, suggesting that the
414 typically circumferential alignment of trabeculae can reduce myocardial stresses.
415 Previous studies by Priya *et al.* showed that the initiation of trabeculation formation
416 relied on a spatial heterogeneity of tissue tension (Priya *et al.*, 2020). It is thus likely
417 that trabeculations modulate stresses where they are formed (Figure 2F) and for
418 their formation to bring about a smoothening of spatial inhomogeneity of wall tissue
419 stiffness as observed in our study (Figure 5B).

420 It should be clarified that although trabeculations forms at 3pdf, and our
421 results show that trabeculations reduce outer curvature tissue stresses, this does not
422 mean that tissue stresses will be lower at 3dpf than 2pdf. Rather, our results show
423 that there is an increase in stresses from 2dpf to the trabeculated 3dpf ventricle, but
424 without the trabeculation (smoothed ventricle) at 3dpf, tissue stresses will be even
425 higher.

426 Our results, however, do not suggest that the presence or absence of the
427 trabeculation cause a catastrophic reduction in cardiac function, in terms of stroke
428 volume or pressure generation (Figure 3F), to be able to explain embryonic lethality
429 in animal models with trabeculation defects. Rather, they suggest that both the
430 trabeculated and non-trabeculated hearts are viable pumps capable of sustaining

431 systemic perfusion needs. As such, inadequate biomechanical function is most likely
432 not the reason for the above-mentioned embryonic lethality.

433 One important issue that our study addresses is the relative role of fluid wall
434 shear stresses induced by fluid drag forces on the endothelial walls and that of
435 ventricular internal tissue tensile and compressive stresses. Many past
436 mechanobiological studies on zebrafish embryos concluded that reduced flow wall
437 shear stress stimuli is the cause for disrupted trabeculation process (Hove *et al.*,
438 2003; Granados-Riveron & Brook, 2012; Boselli *et al.*, 2015; Vedula *et al.*, 2017; Lee
439 *et al.*, 2018; Cavallero *et al.*, 2021; Foo *et al.*, 2021). However, in these scenarios in
440 past studies, the intervention to reduce flow stimuli are likely to have also diminished
441 ventricular pressure and myocardial tissue stresses, and it is not possible to
442 determine the relative importance of the two types of biomechanical stimuli in
443 causing disrupted trabeculation. For example, the use of BDM or blebbistatin to
444 inhibit cardiac contractions or the use of the *weak atrium mutant* (*wea*) will lead to
445 reduced ventricular blood flow, but it will also reduce ventricular pressure and tissue
446 stresses (Lee *et al.*, 2016; Foo *et al.*, 2021), and it is difficult to decouple effects of
447 flow stimuli and wall stress stimuli. In our *gata1*-vasopressin model, the tissue
448 stresses are altered between the *gata1 morphant* before and after vasopressin
449 without significant changes to flow rates, thus enabling a better controlled
450 experiment to determine if ventricular tissue stresses are important for trabeculation.
451 Our vasopressin rescue experiment shows that high tissue stresses can rescue
452 disrupted trabeculation formations and that tissue stresses are indeed important
453 biomechanical stimuli for trabeculation formation (Figure 4A). Our results, however,
454 do not indicate the unimportance of fluid wall shear stresses, and we speculate that

455 both fluid wall shear stresses and ventricular tissue stresses are essential stimuli for
456 proper trabeculation formation.

457 As FE models are not often applied to embryonic hearts, we briefly explain its
458 assumptions and limitations. Our finite element computational model uses previously
459 established methodologies (Shavik *et al.*, 2020; Lashkarinia *et al.*, 2023), which
460 utilizes previously established tissue mechanics theories and computational methods
461 explained in these previous publications. It assumes that the myocardium has a
462 stiffness model that is transversely isotropic and hyperelastic (Guccione *et al.*, 1991),
463 and that at any myocardial location, there is a direction of higher stiffness that
464 corresponds to the myofiber orientation and the direction of maximum shortening.
465 We have further assumed that the myocardium follows the same active tension
466 generation cycle as those observed in canine experiments (Guccione *et al.*, 1993),
467 but with a much smaller magnitude, tuned to fit pressures relevant to zebrafish
468 embryos. The limitation of the modelling is that it is constructed based on theories
469 and measurements from myocardial tissues of other animals, rather than directly
470 from the zebrafish embryo, which might lead to deviations. Further, although the
471 resulting PV loop has reasonable similarity to measured PV loops (Salehin *et al.*,
472 2021), it did not capture a transient early dip in diastole pressure to be negative,
473 which is a limitation, but our conclusion of myocardial stress with regards to
474 trabeculations were made based on simulation results during systole, rather than
475 diastole, and would not be affected.

476 In conclusion, our results suggest that cardiac trabeculae are formed only on
477 the outer curvature of the ventricle as a reaction to the reduced thickness and
478 increased geodesic curvature of the outer curvature walls on the endocardial side.

479 These geometrical changes induce higher tissue stress areas on the outer curvature,
480 so once formed, the role of the trabeculae is to bridge across these areas and
481 reduce the stress burden while retaining the same cardiac function. Our studies also
482 showed that trabeculae formation enabled better deformability, likely enhancing
483 cardiac function, and homogenize spatial variability of ventricular wall stiffnesses.
484 We also showed that high ventricular tissue stresses is important to trabeculae
485 formation via a rescue experiment.

486 **Methods**

487 ***Ethical Approval***

488 Ethical approval for experiments was provided by the Institutional Animal Care
489 and Use Committee at Washington University in St. Louis and the UT Arlington
490 Institutional Animal Care and Use Committee guidelines (IACUC protocols A17.014
491 and A17.016, respectively). Experiments were carried out according to guidelines
492 laid down by these IACUC, and conforms to (Grundy, 2015). All animals have ample
493 access to food, water, and housing.

494 ***Zebrafish Line and Imaging***

495 The zebrafish embryos used in this study were coming from the
496 *Tg(cmlc2:GFP)* line at 2, 3, 4, and 5dpf, in which the targeted GFP is expressed in
497 the myocardial cells allowing for a clear imaging of the zebrafish embryonic
498 myocardium. All embryos used were bred in the animal care facility, and maintained
499 at 28°C. A solution of 0.003% W/V of phenylthiourea in E3 medium was added
500 around 24 hpf to inhibit pigment formation (Salehin *et al.*, 2021).

501 The samples used for the research were imaged in the two different facilities
502 abovementioned, using two different microscopes. In the first, at UT Arlington, the
503 embryos were anesthetized in 0.05% tricaine given to the media and immersed in
504 0.5% low melting point agarose. Before the agarose solidified, the embryos were
505 transferred to a fluorinated ethylene propylene (FEP) tube and vertically mounted on
506 a stage such that the heart was aligned to the imaging light path. Images of the
507 beating zebrafish hearts were acquired using a modified version of SPIM(Huisken &
508 Stainier, 2009; Lee *et al.*, 2016), as described previously(Salehin *et al.*, 2021). GFP
509 excitation was provided by a 473 nm laser and a 20X water dipping objective with a
510 high numerical aperture (NA = 0.5) was used to eliminate spherical aberrations by
511 minimizing refractive index mismatch. The sample was moved along the detection
512 axis while image sequences were captured from the rostral to the caudal end. A
513 Hamamatsu ORCA Flash 4.0 sCMOS camera was used to record 150-280
514 overlapping z-slices with a 10ms exposure time, and each sequence consisted of
515 300 frames (512 x 512 pixels). 4D images were reconstructed by post-acquisition
516 synchronization(Liebling *et al.*, 2005). Tricaine overdose (2%) was used to euthanize
517 animals.

518 In the second facility, at Washington University in St. Louis, embryos were
519 embedded in 1% low-melt agarose by aspiration into a glass capillary. The glass
520 capillary with zebrafish embryo was loaded into the microscope (Zeiss Lightsheet 7)
521 sample chamber, containing E3 media maintained at 28.5° C. The hardened agarose
522 gel cylinder was extruded into the sample chamber and maneuvered into the
523 lightsheet plane until the fluorescent heart myocardium was visible. Image planes
524 were selected and imaged sequentially for the entire volume of the heart using a
525 water immersion 20X objective. At each plane, 500 frames were acquired at an

526 exposure time of 7.5 ms and resolution of $0.23 \mu\text{m}^2/\text{pixel}$ at $2 \mu\text{m}$ z-spacing by a
527 PCO.Edge sCMOS camera (1920 x 1920 pixels, pixel size $6.5 \mu\text{m} \times 6.5 \mu\text{m}$). Actual
528 framerate was 40 ms due to camera readout rate. 4D images were reconstructed by
529 post-acquisition synchronization(Liebling *et al.*, 2005). Embryos were not
530 anesthetized to avoid anaesthetic agent affecting heart function, but environmental
531 conditions were controlled to minimize discomfort. Tricaine overdose (0.5 mg/mL) or
532 hypothermia (20 min in 0°C water) were used to euthanasia.

533 **3D Reconstruction and Motion Tracking**

534 Segmentations of the whole 3D ventricular chambers were conducted with
535 previous methods(Wiputra *et al.*, 2016), via a semi-automatic slice-by-slice approach
536 using a custom-written lazy-snapping algorithm for pixel classification followed by
537 Vascular Modelling ToolKit (VMTK, www.vmtk.org) for surface reconstruction. The
538 models were trimmed, smoothed and prepared using Geomagic Wrap (Geomagic
539 Inc., USA) for the Finite Element simulations. Care was taken not to smooth out finer
540 details of the trabecular layer of the myocardium. Next, cardiac motion tracking was
541 performed using a well-validated cardiac motion estimation algorithm from our
542 previous work (Wiputra *et al.*, 2020). Segmentation was conducted only at one time
543 point, and the reconstructed geometry could be animated to all other time points with
544 the motion field. This motion extraction algorithm involved iterative curve-fitting of a
545 global motion model, the spatial B-splines of temporal Fourier function, onto pair-
546 wise image registration of all consecutive pairs of time points. As Supplementary
547 video 1 can show, motion tracking enabled high fidelity tracking of myocardial
548 boundary motions.

549 **Myocardial Strain Analysis (MSA)**

550 As our algorithm could track image features and not just cardiac structure
551 boundaries, the tracking results could be used for computation of strains, by first
552 computing the 3D deformational gradient tensor using spatial gradients of
553 displacements, before computing the Green-Lagrange strain tensor according to the
554 finite strain theory (Zheng *et al.*, 2022; Ren *et al.*, 2023). We have previously used
555 the algorithm for strain calculations in microscopy and clinical cardiac images (Zheng
556 *et al.*, 2022; Lashkarinia *et al.*, 2023; Ren *et al.*, 2023). The reconstructed end-
557 diastolic models were meshed using ANSYS and converted into a finely detailed
558 volume mesh and strains were evaluated at the nodes of this mesh, as a means of
559 evaluating strains at evenly distributed locations.

560 Direction conventions are demonstrated in Figure 6. Spatially varying radial,
561 circumferential and longitudinal directions were calculated according to previous
562 methods (Zou *et al.*, 2020). At any point in the myocardium, the radial directions
563 were taken as the direction of temperature gradients in a heat transfer simulation
564 from the endocardium to epicardium, the circumferential direction was taken as the
565 cross product of a pre-defined longitudinal axis with the radial direction, while the
566 longitudinal direction was the cross product of radial and circumferential directions.
567 Components of the strain tensors in specific directions were then obtained via
568 projection to those directions.

569 The minimum eigenvector of the strain tensor was computed to obtain the
570 directions of maximum contraction, to inform the direction of contraction in our FE
571 model. This approach was previously used as an approximation of the myocardial
572 fibres direction (Pedrizzetti *et al.*, 2014). To divide the embryonic ventricle into the
573 outer and inner curvature regions, the ventricle was manually and equally divided

574 into two with a slicing plane approximately perpendicular to the atrioventricular inflow
575 direction. n=6 for all groups (2, 3, 4, and 5 pdf).

576 ***Geodesic Curvature Calculation***

577 The 3D reconstruction of the outer curvature of the ventricles was sliced in the
578 circumferential and longitudinal directions. The mid-wall line in between endocardial
579 and epicardial boundaries was extracted and discretized into 100 points. The
580 geodesic curvature of the line at any point was calculated (n=3) as

581
$$\kappa_i = \left\| \frac{dT}{ds} \right\| = \frac{1}{2} \left(\frac{\|T_{i+1}-T_i\|}{\|\alpha_{i+1}-\alpha_i\|} + \frac{\|T_i-T_{i-1}\|}{\|\alpha_i-\alpha_{i-1}\|} \right) \quad (\text{Eq.1})$$

582 Where α_i was the coordinate of the i -th point on the line, s was the distance along
583 the line and T_i was the tangent vector at the i -th point.

584 ***Finite Element Analysis***

585 The mechanical model and finite element (FE) modelling of the zebrafish
586 embryonic ventricle was adapted from previous work (Lashkarinia *et al.*, 2023) and
587 was performed using the open source library FEniCS (<https://fenicsproject.org/>). The
588 source code is available at <https://github.com/WeiXuanChan/heartFEM>. In this FE
589 model, the ventricular stress was modelled as passive stiffness stress and active
590 tension stress.

591 Ventricular tissue passive stiffness was modelled using a Fung-type
592 transversely isotropic hyperelastic constitutive model (strain energy function)
593 (Guccione *et al.*, 1991):

594
$$W = \frac{1}{2} C (e^Q - 1) \quad (\text{Eq.2})$$

595
$$W = \frac{1}{2}C(e^{b_{ff}E_{ff}^2 + b_{xx}(E_{ss}^2 + E_{nn}^2 + E_{sn}^2 + E_{ns}^2) + b_{fx}(E_{fn}^2 + E_{nf}^2 + E_{fs}^2 + E_{sf}^2)} - 1) \quad (\text{Eq.3})$$

596 where E is the Green–Lagrange strain tensor with subscripts f , s , and n
 597 represent myocardial fiber, sheet and sheet normal orientations. We used b_{ff} , b_{xx}
 598 and b_{fx} values as reported by (Ong *et al.*, 2021) for equation 3, but for C , we used
 599 2J/mL for 2dpf and 5J/mL for 3dpf. For the zebrafish embryonic ventricle, the fiber
 600 direction was taken to be the direction of the minimum eigenvector of the strain
 601 tensor, which is the direction of maximum contraction, in accordance with previous
 602 studies (Pedrizzetti *et al.*, 2014). The sheet normal direction was taken to be the
 603 radial direction.

604 The active stress (P_{act}) was prescribed to act in the local fiber direction using
 605 the Guccione active contraction model (Guccione *et al.*, 1993). This is a calcium
 606 activation model that describes the sigmoidal relationship of chemical activation and
 607 tension of the cardiac muscle:

608
$$P_{act} = T_{OLV} \frac{Ca_0^2}{Ca_0^2 + ECa_{50}^2} C_t$$

609 (Eq.4)

610 where T_{OLV} is the maximum tension, Ca_0^2 (peak calcium concentration),
 611 ECa_{50}^2 (calcium sensitivity dependent in the sarcomere length) and C_t (temporal
 612 variation) describe the calcium activation behaviour.

613
$$C_t = \frac{1}{2}(1 - \cos \omega)$$

614 (Eq.5)

615 ω is dependent on the cycle time:

$$616 \quad \omega = \begin{cases} \pi \frac{t}{t_0} & \text{when } 0 \leq t < t_0 \\ \pi \frac{t-t_0+t_r}{t_r} & \text{when } t_0 \leq t < t_0 + t_r \\ 0 & \text{when } t_0 + t_r \leq t \end{cases} \quad (\text{Eq.6})$$

617 where t_0 is the time to peak tension (amount of time that it takes for the myofibers to
 618 contract) and t_r is the relaxation time, calculated as:

$$619 \quad t_r = ml + b \quad (\text{Eq.7})$$

620 where m is the gradient of linear relaxation duration with sarcomere length
 621 relation, b is the time intercept of linear relaxation duration with sarcomere length,
 622 and l is the sarcomere length, dependent on the degree of myocyte stretch.

623 The input geometry for the FE was taken slightly before end-diastolic phase
 624 and from there, the zero-pressure unloaded state of the zebrafish embryonic
 625 ventricle was calculated using a backward displacement method (Finsberg *et al.*,
 626 2018), based on a specified end-diastolic pressure and myocardium stiffness. In
 627 essence, an initial guess of the pressure at the starting input geometry was made,
 628 and this pressure value was iteratively adjusted trying to match the end-diastolic
 629 pressure of the ventricle after pressure loading it to the end-diastolic volume. After
 630 that, an inverse displacement was applied to the starting input geometry, reducing
 631 the ventricle pressure to zero to obtain the estimated unloaded geometry. All the
 632 zebrafish embryonic ventricular models were meshed with a minimum of 5000
 633 quadratic tetrahedral elements, surpassing the previous mesh convergence study
 634 (Ong *et al.*, 2021), in order to retained as many details of the cardiac trabeculae as
 635 possible. The FE simulation was performed using FEniCS, minimizing the

636 Lagrangian cost function detailed by Shavik *et al.* (Shavik *et al.*, 2018). Boundary
637 conditions were weak springs (spring constant = 90 Pa) over the entire epicardial
638 surface emulating the effect of the tissues surrounding the heart, and a constraint at
639 the atrio-ventricular channel (AVC) in the circumferential direction but not in other
640 directions.

641 During the simulations, parameters were adjusted until a reasonable match
642 with experimental and literature measurements of the end-diastolic pressure (EDP),
643 peak systolic pressure and general shape of the P-V loops was achieved (Salehin *et*
644 *al.*, 2021). Specifically, the strain energy function coefficient C (Eq. 2-3, as there are
645 no data available on the stiffness of the zebrafish embryonic ventricle), the time to
646 peak tension t_0 (Eq. 6), the relaxation time t_r (Eq. 7) and the maximum tension T_{OLV}
647 (Eq. 4) were adjusted. C was increased where simulated ventricular pressure was
648 too low, t_0 was elevated where the PV loop did not skew sufficiently to the left, while
649 t_r was reduced if the end-systolic pressure decreased too slowly. A simplified
650 Windkessel model, as shown in Figure Figure 7, was also adopted to model the
651 resistances of flow into and out of the zebrafish embryonic ventricle and pressure
652 dynamics with outflow but was not intended to model other details of the embryonic
653 circulation. This allowed to model systemic flow resistances and compliances to aid
654 realistic pressure and flow rate calculations. The different sets of resistances and
655 compliances in the simplified Windkessel lumped-parameter model were tuned to
656 achieve the expected peak systolic pressures from literature (Salehin *et al.*, 2021)
657 using the stroke volume as imaged, by scaling all resistances and compliances until
658 a match is obtained. The resistance scaling was increased when systemic pressure
659 was too low, while compliance was increased when aortic pulse pressure was too
660 low. FE and Windkessel parameters that enabled a good match are given in Table 2.

661 The zebrafish embryonic ventricular pressure was solved via the coupled FE
662 and lumped-parameter model at each time step over 20 cardiac cycles, and results
663 in the last cycle were used (approach 1). In addition, we performed FE simulations
664 without the lumped-parameter, prescribing the ventricular volume over time
665 waveform as obtained from microscopy images, as a means of obtaining simulated
666 volume over time waveforms that were closer to those from images (approach 2). In
667 both approaches the same FE parameters as shown in Table 2 were used. Results
668 for approach 1 are given in Figure 2 and 3, while results for approach 2 are given in
669 Figure 8A. With approach 2, in the comparison of smoothed, non-trabeculated
670 models to the original trabeculated models, systolic pressures were higher for the
671 smooth models, and it was difficult to judge if the reduced stresses in trabeculated
672 models were due to the presence of trabeculation structures or lower systolic
673 pressure. As such, a third approach was adopted, where the active tension of the
674 smooth models were reduced to ensure that smoothed and trabeculated models
675 have the same peak systolic pressure. Results for approach 3 is given in Figure 8B.
676 n=3 for all approaches.

677 **Gene Knockdown by Morpholinos**

678 The sequence 5'-CTGCAAGTGTAGTATTGAAGATGTC-3' (Gene Tools) was
679 used for the *Gata1* morpholino, that was prepared for injection by dissolving in
680 nuclease free water at 1 mM. One nanoliter MO solution was injected into the yolk
681 adjacent to the cells at the one to four-cell stage. *Gata1* phenotype was confirmed by
682 observing the dorsal aorta for flowing red blood cells after 24 hours post-fertilization
683 (hpf).

684 **Vasopressin Rescue Experiment**

685 Vasopressin (Arginine-Vasopressin Acetate Salt, Sigma, V9879) was
686 dissolved to a concentration of 10 µM in E3 medium (5mM NaCl, 0.17 mM KCl, 0.33
687 mM CaCl₂, 0.33 mM MgSO₄, and 0.1% Methylene Blue) and 0.003% PTU to inhibit
688 pigmentation. *Gata1* MO injected embryos were dechorionated and incubated in
689 vasopressin solution beginning at 24 hpf with replenishment every 24 hours until 4
690 days post-fertilization (dpf).

691 ***Intra-Ventricular Pressure Measurements***

692 These measurements were performed at UT Arlington. 4 embryos for each
693 group (control, gataMO and gataMO with vasopressin treatment) at 4dpf were
694 anesthetized in 0.05% tricaine and placed in an agarose-filled petri dish with
695 customized depressions in the agarose to assist in stabilizing the embryo. Intra-
696 ventricular pressure of zebrafish embryos was measured using a 900A servo null
697 micro-pressure system (World Precision Instruments). 3 measurements were made
698 for each embryo, making n=12. The initial input vacuum and pressure values are
699 given in the 900A Pressure Pod, a part of the 900A Micropressure System, and are
700 delivered and controlled by PV820. was also used to make the tip. The tip's diameter
701 of about 2 to 5 micrometers permitted it to inject into the zebrafish's heart without
702 having any significant damage. The calibration step was crucial for generating an
703 accurate pressure signal before measuring the target sample. A glass electrode
704 (created with WIP's Pul-1000 Four-Step Micropipette Puller) with a tip diameter of 2
705 to 5 micrometers was made of borosilicate glass, filled with 1 M NaCl, and then its tip
706 was put into the ventricle. Changes in ventricular pressure are related to a change in
707 electrical resistance at the micropipette's tip, which is counterbalanced by the
708 system's compensatory positive or negative pressure. Data were recorded at 200
709 samples/second and put through an IIR Butterworth filter with a cut-off frequency

710 calculated from spectral analysis to remove high-frequency noise. A MATLAB
711 (MathWorks) algorithm was used to filter the recorded analogue signals.

712 ***Cannulation and Passive Pressurization of Embryonic Hearts***

713 Passive pressurization experiments were performed at Washington University
714 in St. Louis (n=4 for each of 3 groups, 2dpf control, 3dpf control, and 3dpf gataMO).
715 The atrium was chosen as the point of cannulation as it was more easily accessible,
716 and we needed to avoid damage to the ventricle. pressure equilibrium could be
717 achieved between the atrium and the ventricle due to the proximity, as explained
718 below.

719 Embryos were prepared as follows. Dechorionated embryos were incubated
720 in a 35 mM 2,3-Butanedione monoxime (BDM) solution in E3 to halt heart
721 contractions, which were monitored until cessation. Embryos were then further
722 incubated for approximately 20 minutes to allow for full sarcomere relaxation.
723 Embryos were mounted on a microscope slide within a silicone well. A drop of 1%
724 low-melt agarose in E3 and 35 mM BDM was deposited in the silicone well and
725 embryos were embedded and positioned such that the cannula approached the
726 embryo at a 90° angle. Additionally, embryos were positioned as close to the gel
727 surface as possible to minimize cannula travel through the gel and limit light
728 refraction. A slide with a mounted embryo was inserted into a temperature-controlled
729 microscope stage insert (Bioscience Tools, Highland, CA) while the temperature was
730 maintained at 28.5°C. A long working-distance 40X water immersion objective lens
731 (Olympus, Waltham, MA, LUMPLFLN40XW) on an upright confocal microscope
732 (Olympus, Waltham, MA, FV1000) was lowered until within 1 mm of the gel surface,

733 where it was immersed into a droplet of 35 mM BDM in E3 solution to form a water
734 immersion column.

735 Borosilicate glass capillary tubes were pulled and beveled to a sharp point
736 resulting in a cannula inner diameter of approximately 5 µm by 10 µm (short-axis by
737 long-axis). Cannulae tips were filled with a solution of 1% casein in E3 containing
738 0.2% 0.5 µm red fluorescent beads (Thermo Scientific, Fremont, CA, Fluoro-Max
739 R500) and 25 mM Warfarin (Sigma Aldrich, St. Louis, MO, A4571). Casein prevents
740 the sticking of tissue, while beads allow tracking of flow. Warfarin prevents red blood
741 cell clotting at the cannulation site. Cannulae were prepared in advance to allow the
742 injection solution to back-fill via capillary action, thus filtering the solution to prevent
743 clogging. Additionally, casein requires at least 1 hour to bind to completely block
744 glass surfaces from non-specific binding. After incubation, cannulae were back-filled
745 with E3, warfarin, and bead solution only, displacing the casein solution. A cannula
746 was then attached to a needle holder (World Precision Instruments, inc., Sarasota,
747 FL, MPH315) held by a motorized micromanipulator (Zaber, Vancouver, BC)
748 allowing precise movement of the needle tip. A microfluidic pressure controller
749 (Fluigent, Ile-de-France, France, 25 mbar Flow-EZ) was connected to the cannula to
750 allow precise control of the applied pressure. The microfluidic reservoir was placed
751 near the microscope stage. The reservoir water level must be level with the cannula
752 tip to ensure accurate zero-pressure calibration. Before cannulation, the cannula tip
753 was placed into the immersion water column and lowered to the gel surface. Precise
754 zero pressure was achieved by adjusting the reservoir water level until halting bead
755 flow was observed in the cannula. The cannula tip was then advanced into the
756 embryo sinus venosus region, just posterior to the atrial inlet. Upon puncture of the
757 vasculature, the pressure was again equalized until bead flow was halted.

758 Using the microfluidic pressure controller, the pressure was cycled five times
759 from 0 to 0.5 mmHg and back to zero. This was performed to remove hysteresis in
760 the heart tissue. After pressure cycling, a 3D image stack was acquired which
761 denoted the initial zero-stress state of the cannulated heart. The pressure was then
762 increased at 0.25 mmHg increments, with an equalization period of two minutes
763 between each pressure step. 3D image stacks were acquired after each equalization
764 period. Pressurization was halted when tissue failure or massive leakage was
765 detected. The pressure step before failure was considered the final pressure value,
766 with its corresponding 3D image stack.

767 **Statistical Analysis**

768 All the results in the histograms for the strains were expressed as mean \pm SD.
769 The Wilcoxon signed-rank test was used for hypothesis testing with $p<0.05$
770 considered significant when the data were not normal, while the t-test was used for
771 hypothesis testing with $p<0.05$ considered significant when the data were normally
772 distributed.

773 **References**

- 774 Ahuja N, Ostwald P, Gendernalik A, Guzzolino E, Pitto L, Bark D & Garrity DM. (2022). Myocardial
775 Afterload Is a Key Biomechanical Regulator of Atrioventricular Myocyte Differentiation in
776 Zebrafish. *J Cardiovasc Dev Dis* **9**.
- 777
- 778 Boselli F, Freund JB & Vermot J. (2015). Blood flow mechanics in cardiovascular development. *Cell
779 Mol Life Sci* **72**, 2545-2559.
- 780
- 781 Cairelli AG, Chow RW, Vermot J & Yap CH. (2022). Fluid mechanics of the zebrafish embryonic heart
782 trabeculation. *PLoS Comput Biol* **18**, e1010142.
- 783
- 784 Cavallero S, Blazquez-Medela AM, Satta S & Hsiai TK. (2021). Endothelial mechanotransduction in
785 cardiovascular development and regeneration: emerging approaches and animal models.
786 *Curr Top Membr* **87**, 131-151.

- 787
788 Duchemin AL, Vignes H, Vermot J & Chow R. (2019). Mechanotransduction in cardiovascular
789 morphogenesis and tissue engineering. *Curr Opin Genet Dev* **57**, 106-116.
- 790
791 Finsberg H, Xi C, Tan JL, Zhong L, Genet M, Sundnes J, Lee LC & Wall ST. (2018). Efficient estimation
792 of personalized biventricular mechanical function employing gradient-based optimization.
793 *Int J Numer Method Biomed Eng* **34**, e2982.
- 794
795 Foo YY, Motakis E, Tiang Z, Shen S, Lai JKH, Chan WX, Wiputra H, Chen N, Chen CK, Winkler C, Foo
796 RSY & Yap CH. (2021). Effects of extended pharmacological disruption of zebrafish
797 embryonic heart biomechanical environment on cardiac function, morphology, and gene
798 expression. *Dev Dyn*.
- 799
800 Galloway JL, Wingert RA, Thisse C, Thisse B & Zon LI. (2005). Loss of gata1 but not gata2 converts
801 erythropoiesis to myelopoiesis in zebrafish embryos. *Dev Cell* **8**, 109-116.
- 802
803 Gassmann M, Casagranda F, Orioli D, Simon H, Lai C, Klein R & Lemke G. (1995). Aberrant neural and
804 cardiac development in mice lacking the ErbB4 neuregulin receptor. *Nature* **378**, 390-394.
- 805
806 Gendernalik A, Zebhi B, Ahuja N, Garrity D & Bark D, Jr. (2021). In Vivo Pressurization of the Zebrafish
807 Embryonic Heart as a Tool to Characterize Tissue Properties During Development. *Ann
808 Biomed Eng* **49**, 834-845.
- 809
810 Granados-Riveron JT & Brook JD. (2012). The impact of mechanical forces in heart morphogenesis.
811 *Circ Cardiovasc Genet* **5**, 132-142.
- 812
813 Grundy D. (2015). Principles and standards for reporting animal experiments in The Journal of
814 Physiology and Experimental Physiology, pp. 755-758. Wiley Online Library.
- 815
816 Guccione JM, McCulloch AD & Waldman LK. (1991). Passive material properties of intact ventricular
817 myocardium determined from a cylindrical model. *J Biomech Eng* **113**, 42-55.
- 818
819 Guccione JM, Waldman LK & McCulloch AD. (1993). Mechanics of active contraction in cardiac
820 muscle: Part II--Cylindrical models of the systolic left ventricle. *J Biomech Eng* **115**, 82-90.
- 821
822 Hove JR, Koster RW, Forouhar AS, Acevedo-Bolton G, Fraser SE & Gharib M. (2003). Intracardiac fluid
823 forces are an essential epigenetic factor for embryonic cardiogenesis. *Nature* **421**, 172-177.
- 824
825 Huisken J & Stainier DY. (2009). Selective plane illumination microscopy techniques in
826 developmental biology. *Development* **136**, 1963-1975.
- 827

- 828 Lai D, Liu X, Forrai A, Wolstein O, Michalicek J, Ahmed I, Garratt AN, Birchmeier C, Zhou M, Hartley L,
829 Robb L, Feneley MP, Fatkin D & Harvey RP. (2010). Neuregulin 1 sustains the gene regulatory
830 network in both trabecular and nontrabecular myocardium. *Circ Res* **107**, 715-727.
- 831
- 832 Lashkarinia SS, Chan WX, Motakis E, Ho S, Siddiqui HB, Coban M, Sevgin B, Pekkan K & Yap CH.
833 (2023). Myocardial Biomechanics and the Consequent Differentially Expressed Genes of the
834 Left Atrial Ligation Chick Embryonic Model of Hypoplastic Left Heart Syndrome. *Ann Biomed
835 Eng* **51**, 1063-1078.
- 836
- 837 Lee J, Chou TC, Kang D, Kang H, Chen J, Baek KI, Wang W, Ding Y, Carlo DD, Tai YC & Hsiai TK. (2017).
838 A Rapid Capillary-Pressure Driven Micro-Channel to Demonstrate Newtonian Fluid Behavior
839 of Zebrafish Blood at High Shear Rates. *Sci Rep* **7**, 1980.
- 840
- 841 Lee J, Fei P, Packard RR, Kang H, Xu H, Baek KI, Jen N, Chen J, Yen H, Kuo CC, Chi NC, Ho CM, Li R &
842 Hsiai TK. (2016). 4-Dimensional light-sheet microscopy to elucidate shear stress modulation
843 of cardiac trabeculation. *J Clin Invest* **126**, 1679-1690.
- 844
- 845 Lee J, Vedula V, Baek KI, Chen J, Hsu JJ, Ding Y, Chang CC, Kang H, Small A, Fei P, Chuong CM, Li R,
846 Demer L, Packard RRS, Marsden AL & Hsiai TK. (2018). Spatial and temporal variations in
847 hemodynamic forces initiate cardiac trabeculation. *JCI Insight* **3**.
- 848
- 849 Liebling M, Forouhar AS, Gharib M, Fraser SE & Dickinson ME. (2005). Four-dimensional cardiac
850 imaging in living embryos via postacquisition synchronization of nongated slice sequences. *J
851 Biomed Opt* **10**, 054001.
- 852
- 853 Liu J, Bressan M, Hassel D, Huisken J, Staudt D, Kikuchi K, Poss KD, Mikawa T & Stainier DY. (2010). A
854 dual role for ErbB2 signaling in cardiac trabeculation. *Development* **137**, 3867-3875.
- 855
- 856 Miller LA. (2011). Fluid dynamics of ventricular filling in the embryonic heart. *Cell Biochem Biophys*
857 **61**, 33-45.
- 858
- 859 Ong CW, Ren M, Wiputra H, Mojumder J, Chan WX, Tulzer A, Tulzer G, Buist ML, Mattar CNZ, Lee LC
860 & Yap CH. (2021). Biomechanics of Human Fetal Hearts with Critical Aortic Stenosis. *Ann
861 Biomed Eng* **49**, 1364-1379.
- 862
- 863 Pedrizzetti G, Sengupta S, Caracciolo G, Park CS, Amaki M, Goliasch G, Narula J & Sengupta PP.
864 (2014). Three-dimensional principal strain analysis for characterizing subclinical changes in
865 left ventricular function. *J Am Soc Echocardiogr* **27**, 1041-1050. e1041.
- 866
- 867 Priya R, Allanki S, Gentile A, Mansingh S, Uribe V, Maischein HM & Stainier DYR. (2020). Tension
868 heterogeneity directs form and fate to pattern the myocardial wall. *Nature* **588**, 130-134.
- 869

- 870 Rasouli SJ & Stainier DYR. (2017). Regulation of cardiomyocyte behavior in zebrafish trabeculation by
871 Neuregulin 2a signaling. *Nat Commun* **8**, 15281.
- 872
- 873 Ren M, Chan WX, Green L, Armstrong A, Tulzer A, Tulzer G, Buist ML & Yap CH. (2023). Contribution
874 of Ventricular Motion and Sampling Location to Discrepancies in Two-Dimensional Versus
875 Three-Dimensional Fetal Ventricular Strain Measures. *J Am Soc Echocardiogr*.
- 876
- 877 Salehin N, Teranikar T, Lee J & Chuong CJ. (2022). Ventricular anisotropic deformation and
878 contractile function of the developing heart of zebrafish *in vivo*. *Dev Dyn*.
- 879
- 880 Salehin N, Villarreal C, Teranikar T, Dubansky B, Lee J & Chuong CJ. (2021). Assessing Pressure-
881 Volume Relationship in Developing Heart of Zebrafish *In-Vivo*. *Ann Biomed Eng* **49**, 2080-
882 2093.
- 883
- 884 Samsa LA, Yang B & Liu J. (2013). Embryonic cardiac chamber maturation: Trabeculation, conduction,
885 and cardiomyocyte proliferation. *Am J Med Genet C Semin Med Genet* **163C**, 157-168.
- 886
- 887 Shavik SM, Jiang Z, Baek S & Lee LC. (2018). High Spatial Resolution Multi-Organ Finite Element
888 Modeling of Ventricular-Arterial Coupling. *Front Physiol* **9**, 119.
- 889
- 890 Shavik SM, Tossas-Betancourt C, Figueira CA, Baek S & Lee LC. (2020). Multiscale modeling
891 framework of ventricular-arterial bi-directional interactions in the cardiopulmonary
892 circulation. *Front Physiol* **11**, 2.
- 893
- 894 Srivastava D & Olson EN. (2000). A genetic blueprint for cardiac development. *Nature* **407**, 221-226.
- 895
- 896 Staudt DW, Liu J, Thorn KS, Stuurman N, Liebling M & Stainier DY. (2014). High-resolution imaging of
897 cardiomyocyte behavior reveals two distinct steps in ventricular trabeculation. *Development*
898 **141**, 585-593.
- 899
- 900 Teranikar TA, Villarreal, C., Salehin, N., Ijaseun, T., Lim, J., Cao, H., Chuong, C., & Lee, J. (2021).
901 Feature Detection to Segment Cardiomyocyte Nuclei for Investigating Cardiac Contractility.
902 *SSRN Electronic Journal*.
- 903
- 904 Utagikar MM & Naik S. (2013). Finite element analysis of elliptical pressure vessels. *AJER, ISSN*, 2320-
905 0847.
- 906
- 907 Vedula V, Lee J, Xu H, Kuo CJ, Hsiao TK & Marsden AL. (2017). A method to quantify mechanobiologic
908 forces during zebrafish cardiac development using 4-D light sheet imaging and
909 computational modeling. *PLoS Comput Biol* **13**, e1005828.
- 910

- 911 Wiputra H, Chan WX, Foo YY, Ho S & Yap CH. (2020). Cardiac motion estimation from medical
912 images: a regularisation framework applied on pairwise image registration displacement
913 fields. *Sci Rep* **10**, 18510.
- 914
- 915 Wiputra H, Lai CQ, Lim GL, Heng JJ, Guo L, Soomar SM, Leo HL, Biwas A, Mattar CN & Yap CH. (2016).
916 Fluid mechanics of human fetal right ventricles from image-based computational fluid
917 dynamics using 4D clinical ultrasound scans. *Am J Physiol Heart Circ Physiol* **311**, H1498-
918 H1508.
- 919
- 920 Zheng Y, Chan WX, Charles CJ, Richards AM, Lee LC, Leo HL & Yap CH. (2022). Morphological,
921 functional, and biomechanical progression of LV remodelling in a porcine model of HFpEF. *J
922 Biomech* **144**, 111348.
- 923
- 924 Zou H, Leng S, Xi C, Zhao X, Koh AS, Gao F, Tan JL, Tan RS, Allen JC, Lee LC, Genet M & Zhong L.
925 (2020). Three-dimensional biventricular strains in pulmonary arterial hypertension patients
926 using hyperelastic warping. *Comput Methods Programs Biomed* **189**, 105345.
- 927

928 Additional Information

929 Data Availability Statement

930 4D images, reconstructed embryonic heart anatomic models, and a list of
931 parameters used for all simulations are available at
932 <https://doi.org/10.5281/zenodo.10323795>. The source code for Finite Element
933 Analysis and modelling is already available
934 at <https://github.com/WeiXuanChan/heartFEM>, while motion tracking code for
935 myocardial strain analysis is available at
936 <https://github.com/WeiXuanChan/motionSegmentation>.

937 Competing Interests

938 The authors declare that the research was conducted in the absence of any
939 commercial or financial relationship that could be construed as a potential conflict of
940 interest.

941 **Authors Contributions**

942 A.G.C., C.H.Y, D.B. and J.V. designed research. A.G.C., A.G., W.X.C, P.N.
943 and J.L. performed research and analysed data. A.G.C and C.H.Y. wrote the paper.
944 All authors contributed to the manuscript revision and read and approved the
945 submitted version. All authors approved the final version of the manuscript and agree
946 to be accountable for all aspects of the work in ensuring that questions related to the
947 accuracy or integrity of any part of the work are appropriately investigated and
948 resolved. All persons designated as authors qualify for authorship, and all those who
949 qualify for authorship are listed.

950 **Fundings**

951 This study is supported by the Imperial College PhD Scholarship for
952 supporting AGC, Imperial College startup funding (CHY). All funders have no role in
953 study design, data collection and analysis, decision to publish, or preparation of the
954 manuscript.

955 **Figure Legends**

956 **Abstract Figure –** Cardiac trabeculae have several roles in the cardiovascular development and
957 function. The first role is the enhancement of tissue deformability in the outer curvature of the
958 ventricle; the second role is the reduction in myocardial tissue stress; the third role is homogenization
959 of wall stiffness. The cardiac trabeculae and tissue stresses are very interconnected: when the tissue
960 stresses are absent or reduced, the trabeculae fail to form properly in the tissue; when a non-
961 trabeculated ventricle is stimulated with high stress, the cardiac trabeculae are restored.

962

963 **Figure 1 – High myocardial strains at the outer curvature zone and at trabeculae.** (A)
964 Microscopy images and 3D anatomic reconstruction of the developing zebrafish embryonic
965 myocardium. Representative segmentation of the ventricle (left) and a single trabecular cluster (right),
966 superimposed on the raw images, at 25%, 50%, and 75% of the cardiac cycle. The 3D reconstructed
967 volumes are in red, while the regions of the 3D reconstruction close to the plane of the shown image
968 are plotted in cyan on single 2D slice extracted from 4D image stacks of a zebrafish embryo from the
969 *Tg(cm1c2:GFP)* line at 3 dpf. A, atrium; V, ventricle; ITS, intra-trabecular space; T, trabecula. Here, t
970 denotes time, while T denotes cardiac cycle duration. (B) 3D reconstruction of a representative
971 zebrafish embryonic ventricle divided into the inner curvature zone (blue) and the outer curvature

972 zone (gray). **(C)** Systole-diastole spatially averaged myocardial strain results for the two zones ($n=6$
973 for each developmental stage). The red dashed line separated the pre-trabecular stage, 2dpf, from
974 the trabecular stage, from 3dpf on. **(D)** 3D reconstruction of a representative single trabecular cluster
975 taken from the outer curvature zone of the ventricle, where trabeculae are formed. **(E)** Myocardial
976 strain results for single trabecular clusters, comparing strains of trabeculae to those of inter-trabecular
977 myocardium. Strains are quantified in the direction of myofiber alignment, and spatially averaged ($n=6$
978 for bar plot). * $p<0.05$ between inner curvature and outer curvature zones, and between trabeculae
979 and inter-trabecular myocardium.

980

981 **Figure 2 – Ventricular geometry and myocardial stress changes during formation of cardiac**
982 **trabeculae.** **(A)** 3D reconstructions of a 2dpf and a 3dpf zebrafish embryonic ventricles. Three
983 circumferential planes (black dotted lines) near the middle of the ventricle were used for geodesic
984 curvature evaluation, which are plotted in Figure 2C. **(B)** Myocardial wall geodesic curvature is
985 evaluated from the circumferential mid-wall line (dashed line) for the outer curvature zone (grey). **(C)**
986 Spatially averaged circumferential myocardial geodesic curvature at the middle of the outer curvature
987 zone of the ventricle from 2dpf to 5dpf ($n=6$ for each developmental stage). **(D)** 3D reconstruction of
988 the hearts, boxed area demonstrates the part on the outer curvature region where myocardial
989 thickness is assessed in (E). **(E)** Estimation of the myocardial thickness at the outer curvature zone of
990 the ventricle from 2 to 5dpf ($n=6$ for each developmental stage). **(F)** Color Contour plots of the Cauchy
991 stress magnitude as extracted from the FE simulation at 2dpf and 3dpf (pre-trabecular versus
992 trabeculated stages), demonstrating an accumulation of stresses on the myocardial walls at the outer
993 curvature zone at 3dpf. **(G)** Spatially averaged Cauchy Stress for 2dpf (dotted line) and 3dpf (solid
994 line) embryos from FE simulations, for the inner curvature zone (blue) and outer curvature zone
995 (grey). **(H)** Spatially averaged strains in the fiber direction for 2dpf (dotted line) and 3dpf (solid line)
996 embryos from FE simulations, for the inner curvature zone (blue) and outer curvature zone (grey).
997 * $p<0.05$.

998 **Figure 3 – Cardiac trabeculae reduce overall stress burden on the myocardial walls.** **(A)**
999 Geodesic curvature of the outer curvature zone is higher in the circumferential direction compared to
1000 the longitudinal direction ($n=3$). **(B)** Circumferential and longitudinal Cauchy stresses of the 3dpf
1001 ventricle, averaged over entire ventricle and over the cardiac cycle, from FE simulations, assuming all
1002 myofibers are aligned longitudinally (left) or circumferentially (right). Circumferential alignment of
1003 myofibers reduce myocardial tissue stresses, suggesting that the circumferential alignment of
1004 trabeculations can similarly reduce stresses ($n=3$). **(C)** Spatially averaged, end-diastolic, whole heart
1005 myocardial tissue stresses in the circumferential and longitudinal directions, from FE Simulations, due
1006 to diastolic passive pressure loading of the 3dpf ventricle. Circumferential tissue stresses are higher,
1007 suggesting a need for circumferential structural support ($n=3$). **(D)** 3D reconstruction of the outer
1008 curvature zone of a normal, trabeculated 3dpf ventricle, and its artificially smoothed-out version with
1009 the same myocardial mass, for use in FE simulations. **(E)** Color contour plots of Cauchy stress tensor
1010 magnitude of the same ventricles in (D) from FE simulations, from the lateral view. The presence of
1011 trabeculae appears to reduce stress concentration on the outer curvature walls (dotted box). **(F)**
1012 Pressure-volume loops comparing the smooth and trabeculated ventricles for the FE simulations in
1013 (E), performed with the same Windkessel circuit. **(G)** Spatially averaged Cauchy stresses over cardiac
1014 cycle for the FE simulations in (E). **(H)** Ratio of temporal peak, spatially averaged Cauchy stress of
1015 the smooth model over that of the trabeculated model, for the three 3dpf ventricles ($n=3$). The red
1016 dashed line indicates a ratio of 1. Stress burden is higher in smooth models than trabeculated models,
1017 confirming the role of trabeculae to reduce the overall tissue stress burden on the myocardial walls. **(I)**
1018 Top row: spatially averaged Cauchy stress magnitude in the circumferential and longitudinal
1019 directions for three embryonic samples at 2dpf, before the formation of trabeculae. Bottom row:
1020 spatially averaged Cauchy stress magnitude in the circumferential and longitudinal directions for three
1021 embryonic samples at 3dpf, after the formation of trabeculae. * $p<0.05$

1022

1023 **Figure 4 – Vasopressin treatment can rescue disruption to trabeculae formation in gata1MO.**
1024 **(A)** Representative microscopic images of 4dpf control zebrafish embryo, gata1 morphant and

1025 vasopressin-treated gata1 morphant. Cardiac trabeculae are reduced in the gata1MO but are rescued
1026 after vasopressin treatment. **(B)** Demonstration of delineation of the compact layer (red) and
1027 trabecular layer (green) used for quantification in (C). **(C)** Manual quantification of 3D trabecular and
1028 compact myocardium volumes for control, gata1MO and vasopressin treated gata1MO ($n=10$). **(D)**
1029 Servo-null measurements of peak intra-ventricular pressures of controls, gata1 morphants and
1030 vasopressin-treated gata1 morphants at 4dpf ($n=12$, 3 measurements for each of 4 embryos per
1031 group). **(E)** Pressure-volume loops of the trabeculated 3dpf ventricle from FE simulations assuming
1032 control group pressure compared to FE simulations assuming gata1MO pressure and gata1MO with
1033 vasopressin treatment pressure. Simulations are performed with a Windkessel circuit, resistance
1034 components of the circuit for the gata1MO simulation are scaled down by the ratio of peak pressure
1035 between controls and gata1MO from (D), while compliance components are scaled up by the same,
1036 so that peak pressure from simulations will match values in (D). Analogous for the gata1MO with
1037 vasopressin. **(F)** Spatially averaged Cauchy stress tensor magnitude over time for simulations in (E).
1038 * $p<0.05$

1039

1040 **Figure 5 – Cardiac trabeculae help ensure spatial homogenization of the ventricular wall**
1041 **stiffness.** Areal stretch difference contour plots for 2dpf normal embryonic ventricle, a 3dpf normal
1042 embryonic ventricle, and a 3dpf Gata1MO embryonic ventricle. In the normal ventricle, bands of
1043 different stiffnesses are visible at 2dpf, but disappear after the formation of cardiac trabeculae at 3dpf.
1044 In the Gata1MO ventricles, where trabeculation formation is disrupted, bands of different stiffness are
1045 still present.

1046

1047 **Figure 6 – Orthogonal axes for the 3D strain analysis.** 3D reconstruction of the ventricular
1048 myocardium with atrioventricular channel (AVC) and outflow tract (OFT) labelled. Computed
1049 circumferential (red), longitudinal (blue) and radial (green) directions are plotted on the ventricle.

1050

1051 **Figure 7 – Simplified Windkessel circuit used in the FE simulations.** V is the volume, P is the
1052 pressure, R is the resistance, C is the compliance, q is the flow. PER stands for peripheral, AO stands
1053 for aortic, VEN stands for venous, MV stands for mitral valve, LA stands for left atrium, LV stands for
1054 left ventricle.

1055

1056 **Figure 8 – Cardiac trabeculae reduce the overall tissue stress burden on the myocardial walls.**
1057 (A) Top row: pressure-volume loops comparing the smooth and trabeculated ventricular models from
1058 FE simulations performed using the approach 1 (volume constraint FE) with the same simulation
1059 parameters for both models. Bottom row: spatially averaged Cauchy stress magnitude over time.
1060 Each column represents an embryonic sample. (B) Top row: pressure-volume loops comparing the
1061 smooth and trabeculated ventricular models from FE simulations performed using the approach 2
1062 (volume constraint FE) with the maximum tension reduced to match the peak pressure in both
1063 trabeculated and smooth models. Bottom row: spatially averaged Cauchy stress magnitude over time.
1064 Each column represents an embryonic sample.

1065

1066 **Tables**

1067 **Table 1 – The formation of trabeculae homogenizes the ventricular wall stiffness.** Spatial
1068 standard deviation of the ventricular wall areal stretch difference (indicating ventricular wall stiffness)
1069 for controls, gata1MO and vasopressin treated gata1MO groups ($n=4$ each).

SD 2dpf Control	SD 3dpf Control	SD 2dpf GataMO
0.093	0.060	0.173
0.083	0.075	0.084
0.101	0.054	0.063
0.103	0.061	0.096

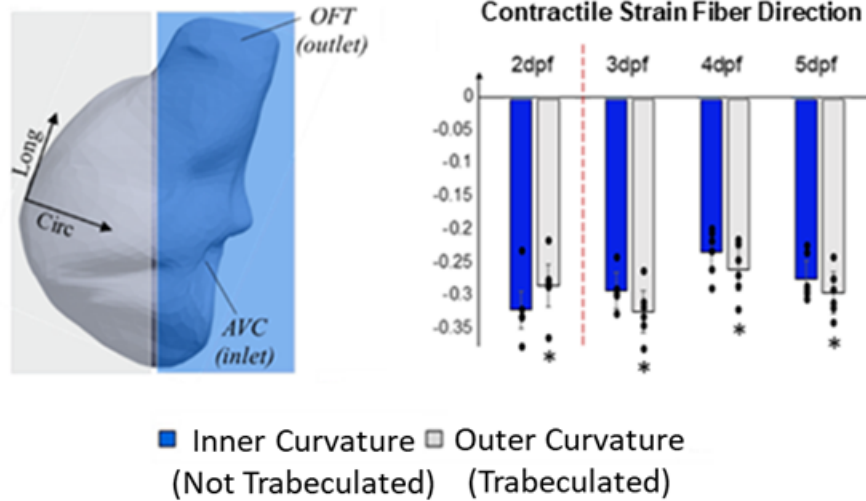
1070

1071 **Table 2 – Modeling parameters for the Finite Element simulations.** The parameters shown were
 1072 either taken from literature or tuned until a good match between simulated and experimental P-V
 1073 loops was reached.

	2dpf	3dpf
<i>Cardiac cycle length [ms]</i>	700	550
<i>Time to peak tension [ms]</i>	220	175
<i>Active tension force [Pa]</i>	4000	7500
<i>End-diastolic pressure [mmHg]</i>	1.36	1.36
<i>Strain energy function coefficient [Pa]</i>	2000	5000
<i>Aortic valve resistance [mmHg*sec*mL⁻¹]</i>	-	0.7118
<i>Peripheral resistance [mmHg*sec*mL⁻¹]</i>	-	4.5
<i>Venous resistance [mmHg*sec*mL⁻¹]</i>	-	0.005
<i>Mitral valve resistance [mmHg*sec*mL⁻¹]</i>	-	0.0101
<i>Aortic compliance [mL/mmHg]</i>	-	0.0117
<i>Venous compliance [mL/mmHg]</i>	-	3.5948
<i>Left atrium compliance [mL/mmHg]</i>	-	0.0018

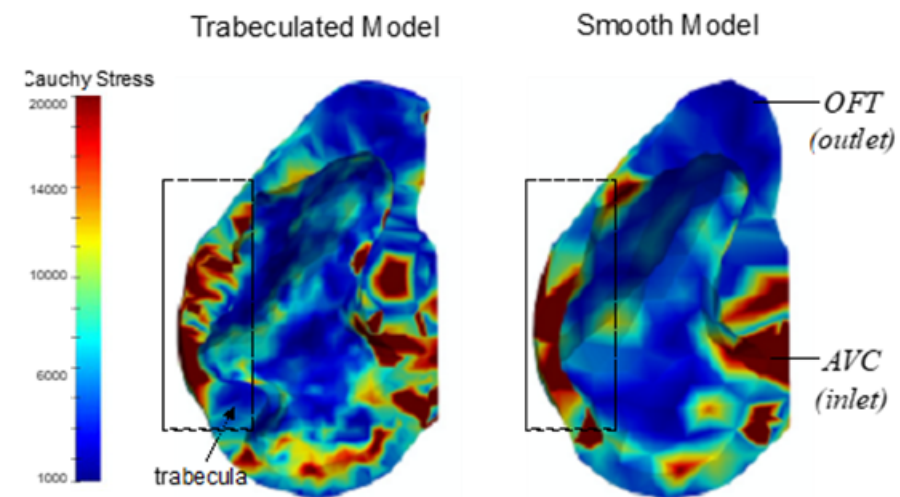
1074

1



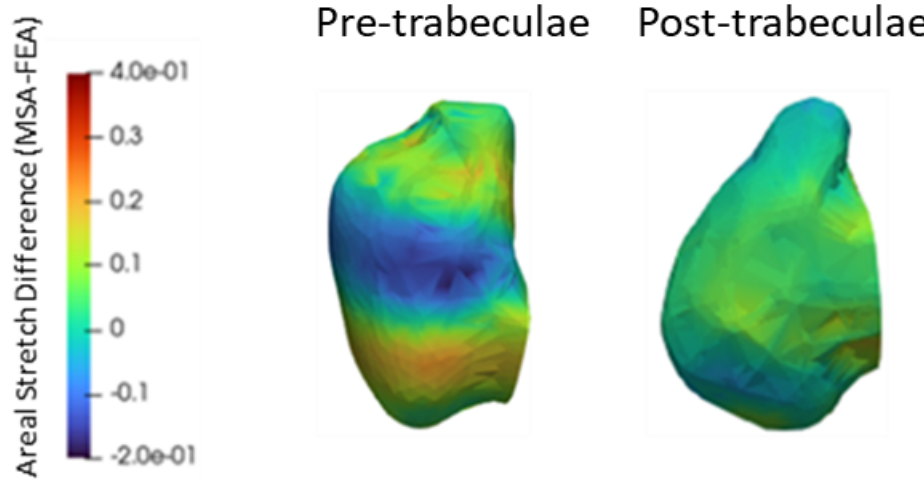
Trabeculae enhance tissue deformability

2



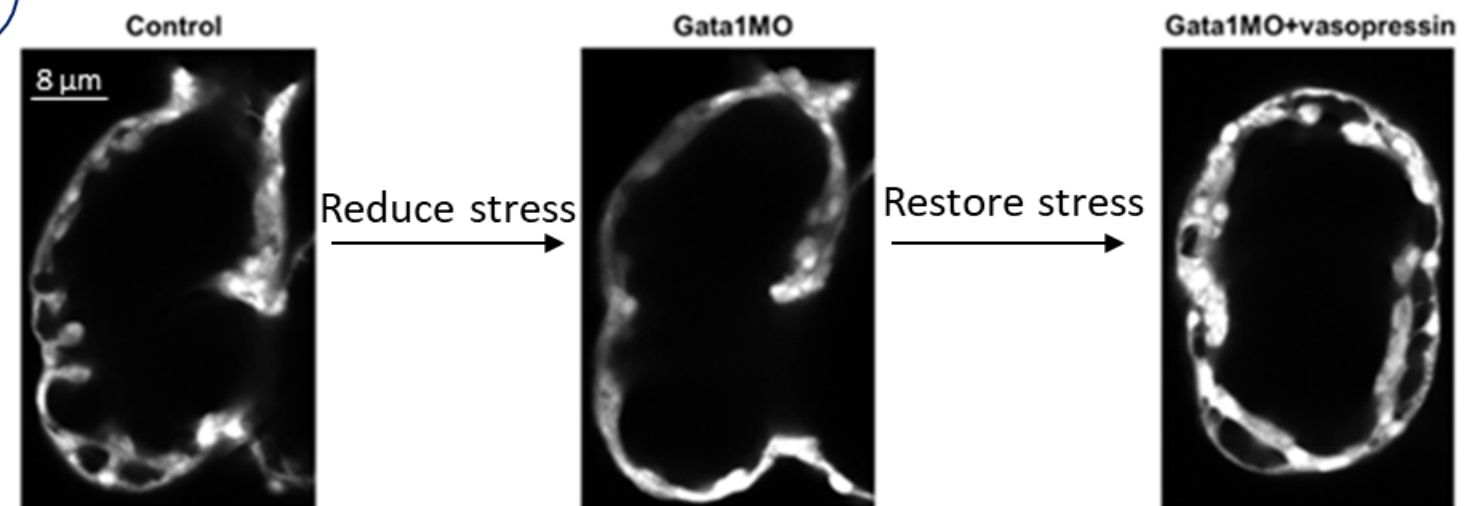
Trabeculae reduce myocardial tissue stresses

3

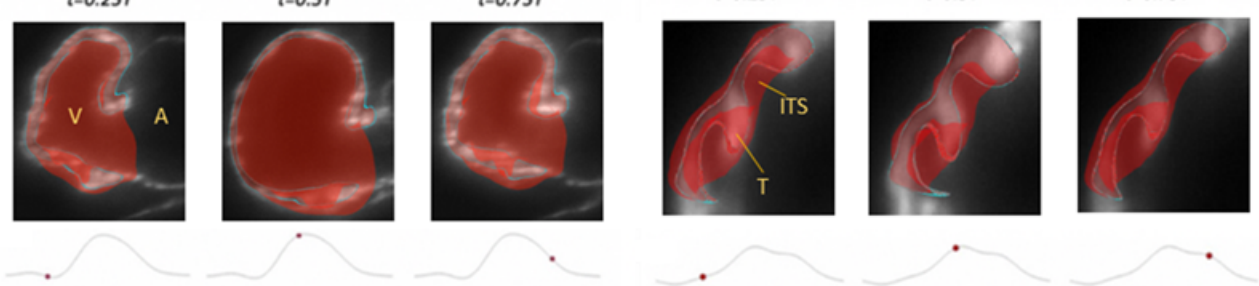
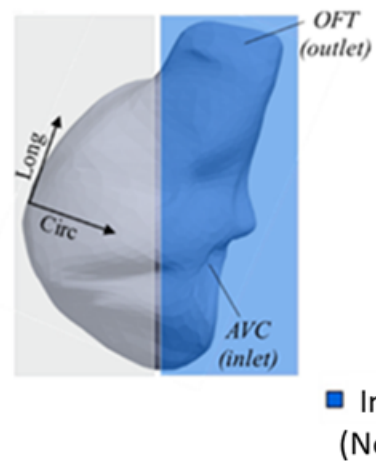


Trabeculae homogenize wall stiffness

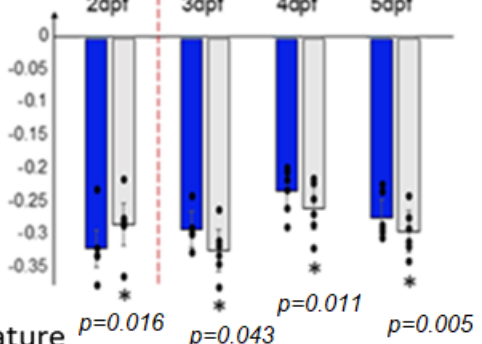
4



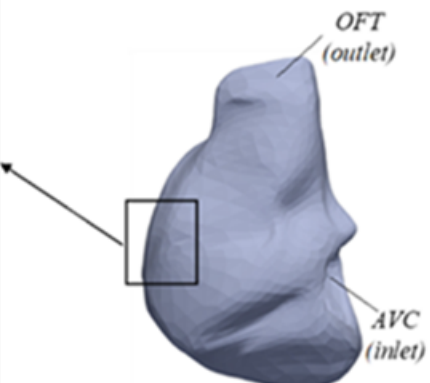
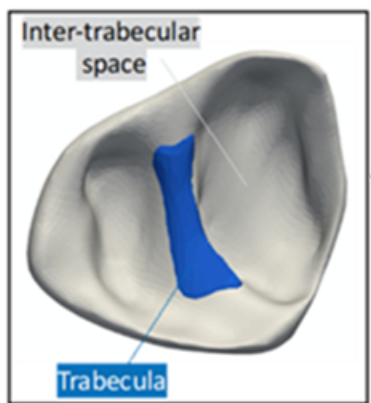
Myocardial tissue stresses important for trabeculae formation

A**B****C**

Contractile Strain Fiber Direction



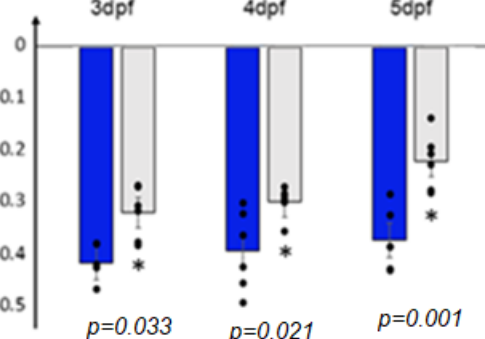
■ Inner Curvature □ Outer Curvature
(Not Trabeculated) (Trabeculated)

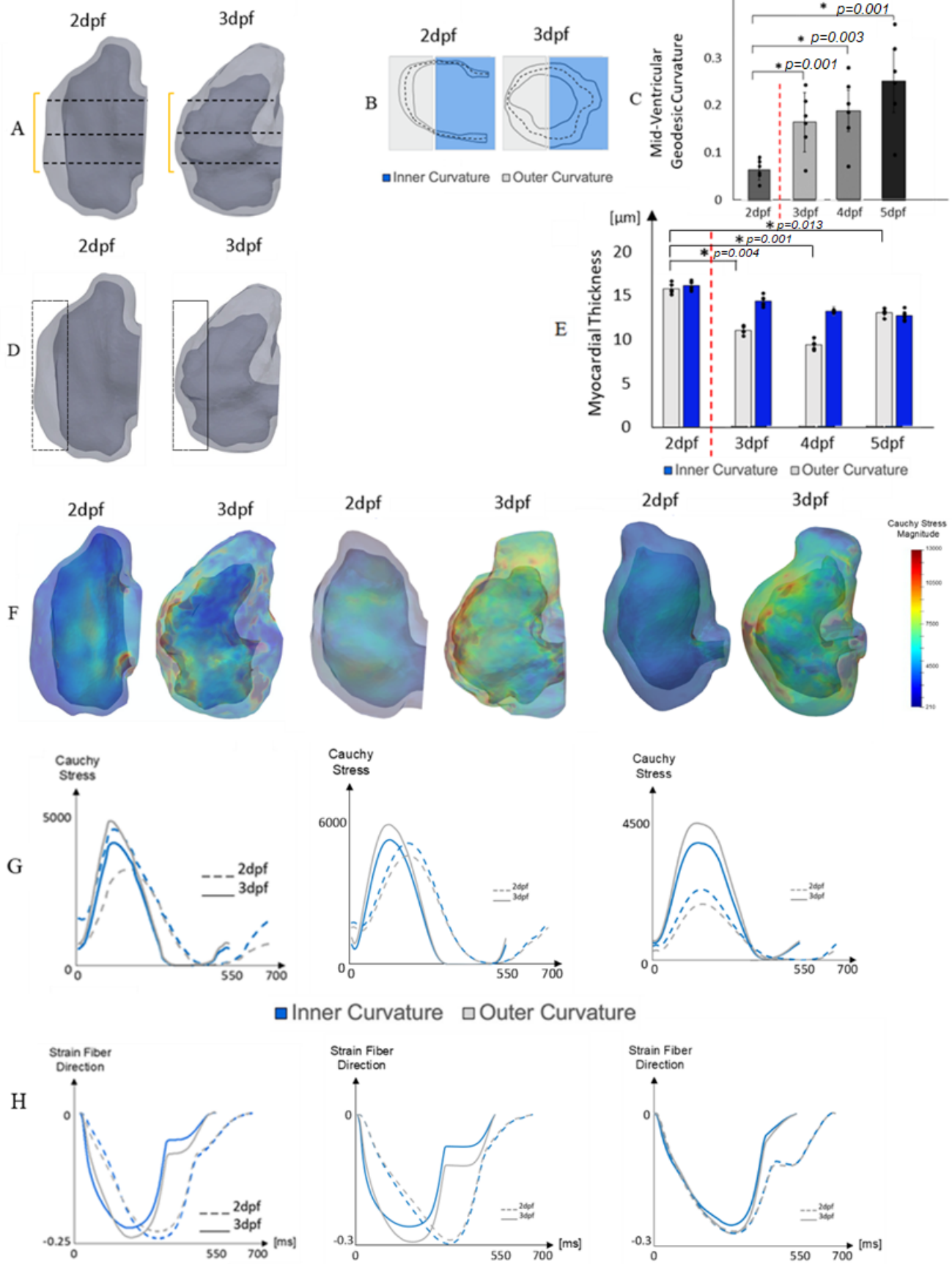
D

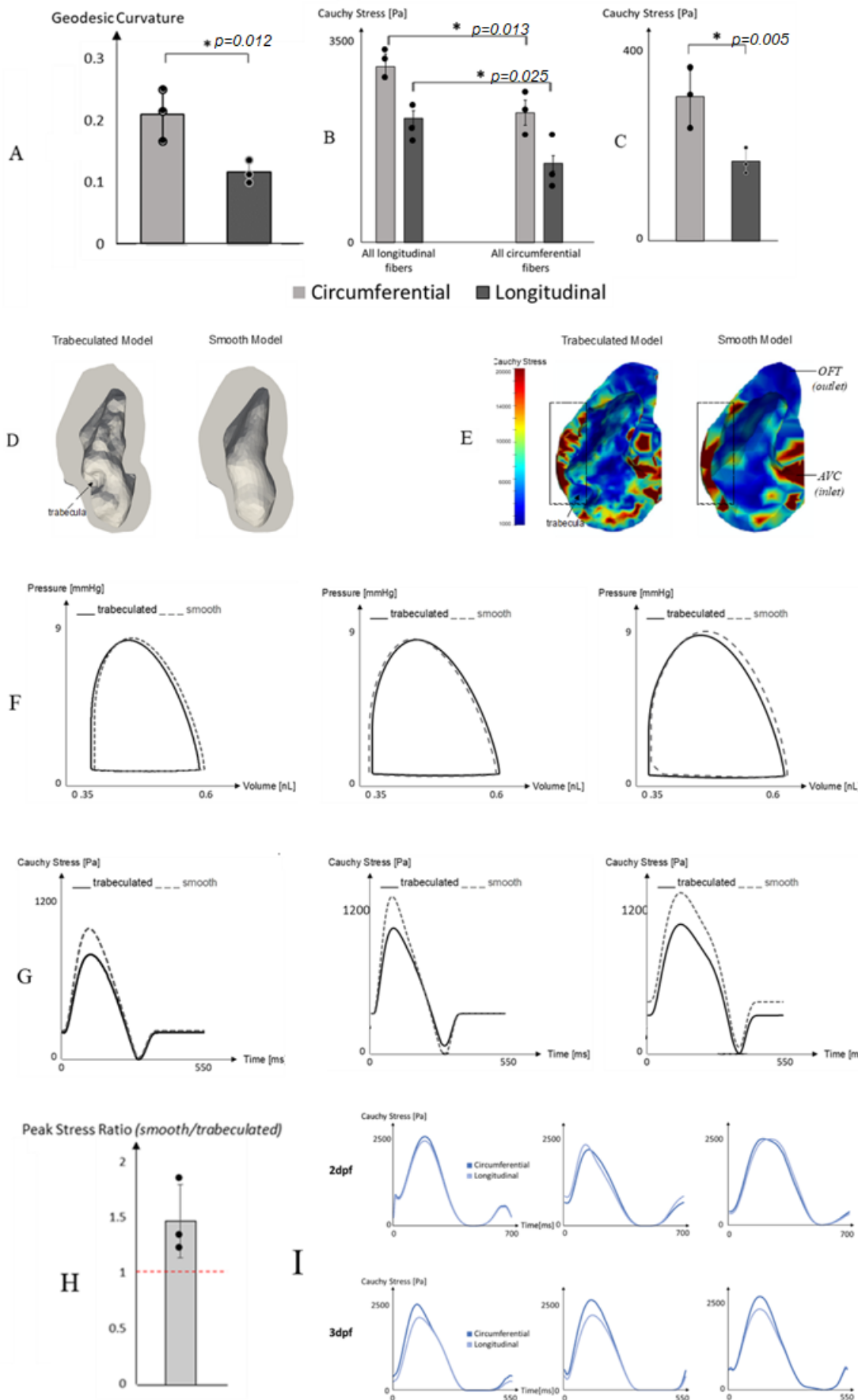
■ Trabeculae □ Inter-Trabecular Myocardium

E

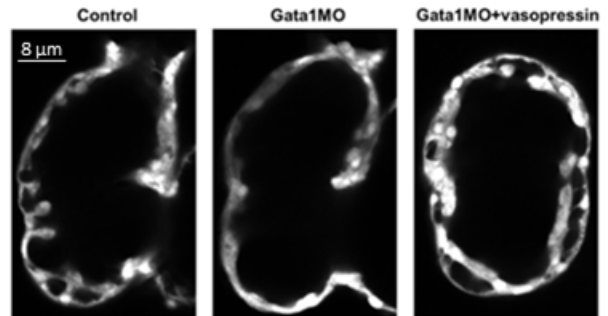
Contractile Strain Fiber Direction



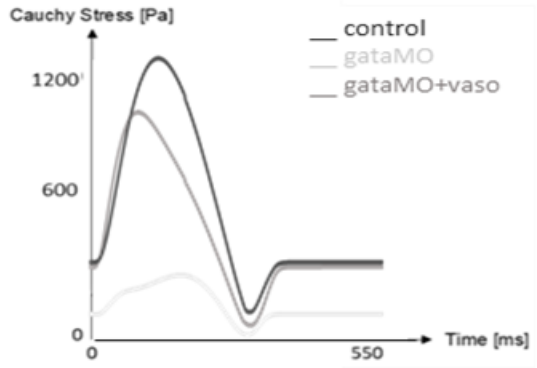
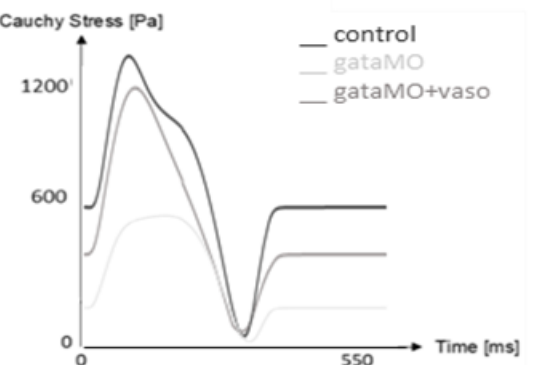
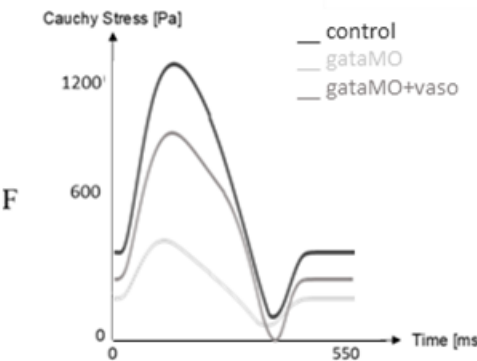
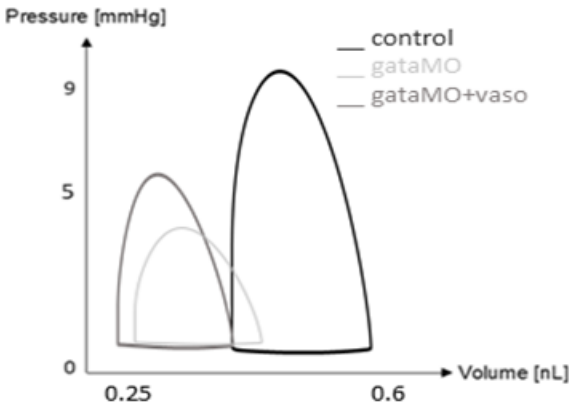
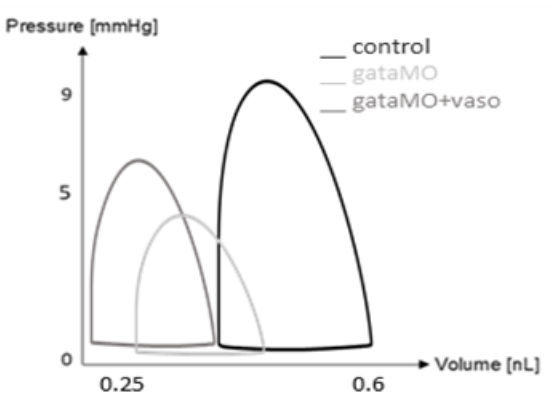
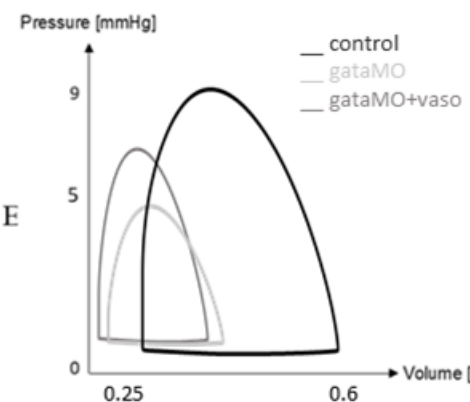
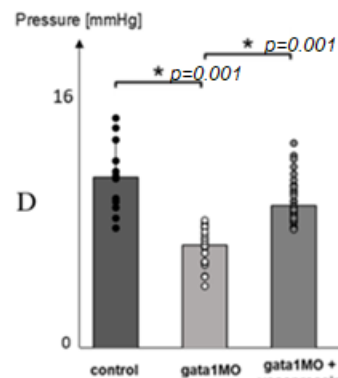
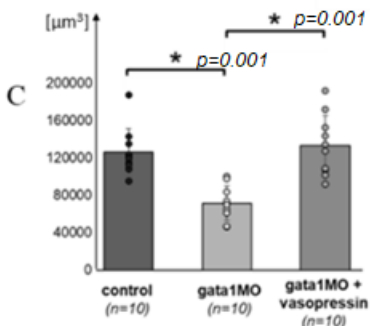
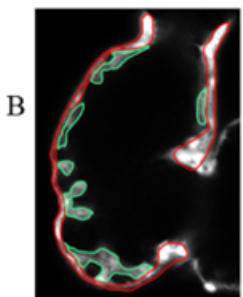


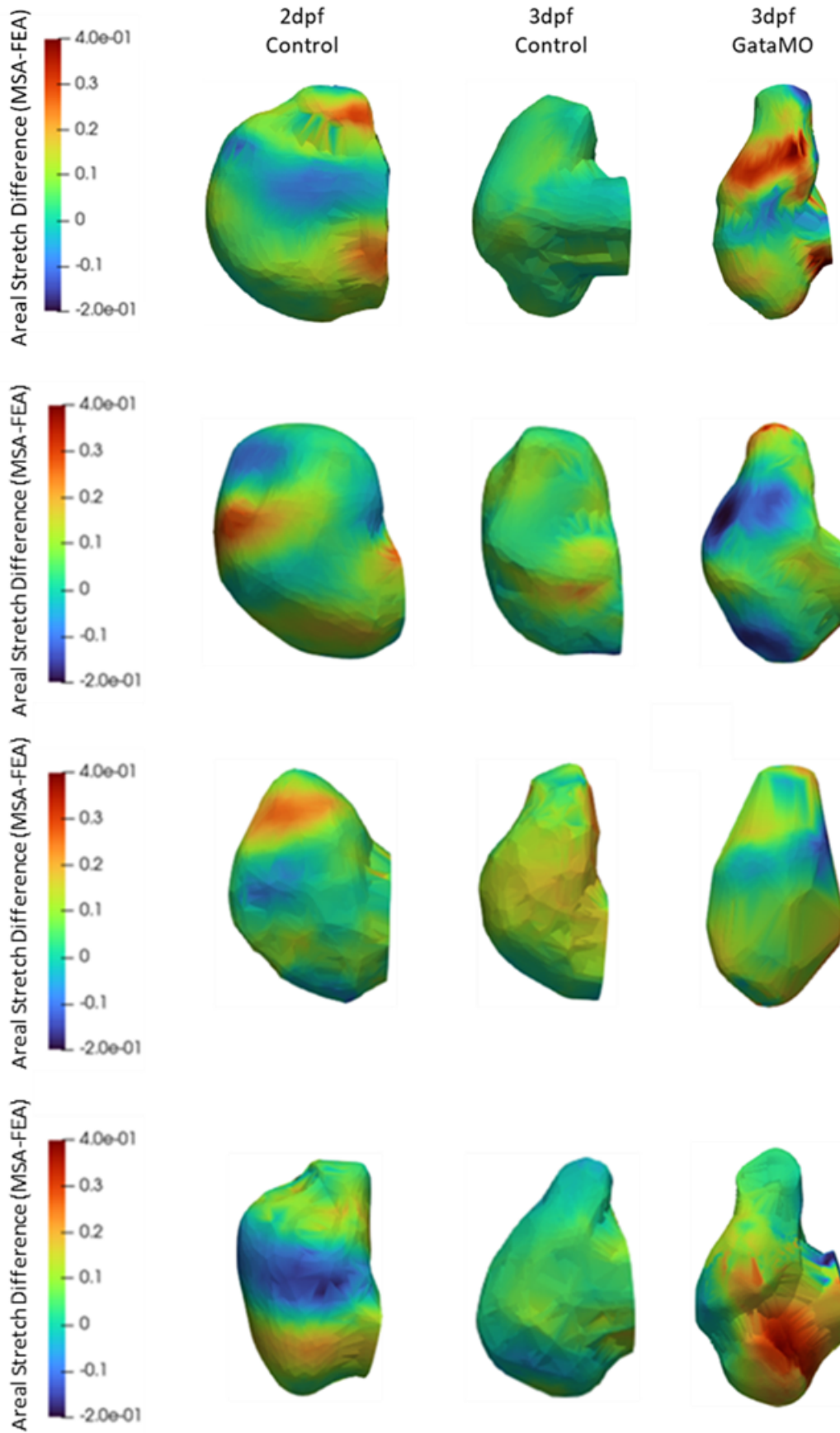


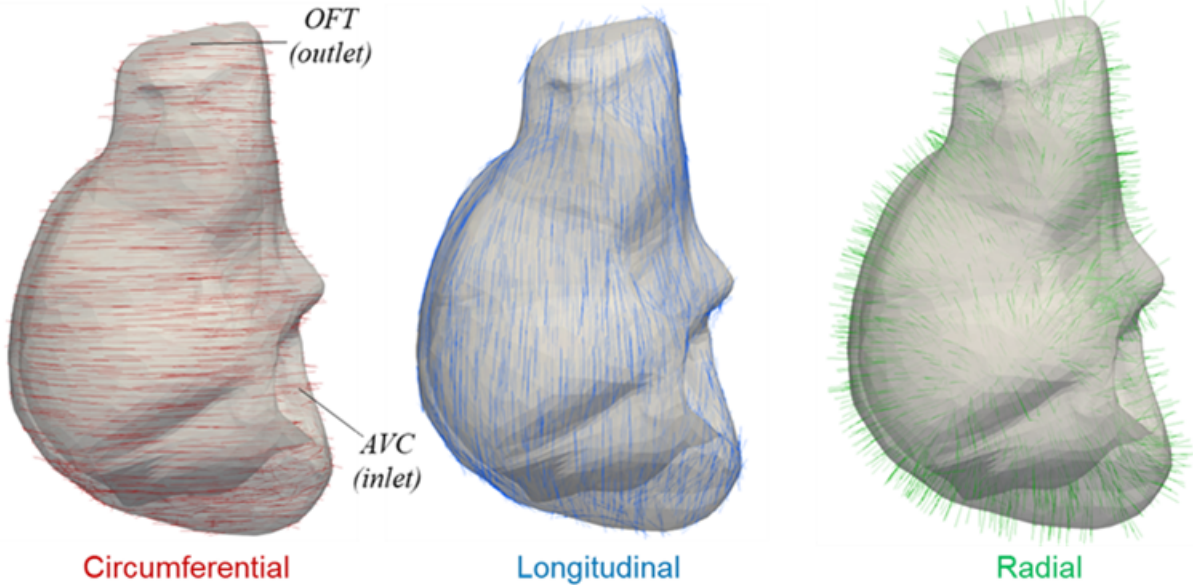
Rescue Experiment

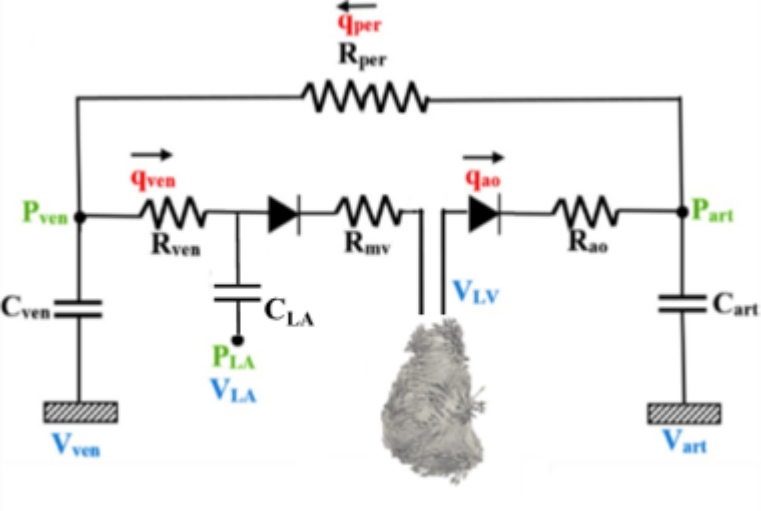


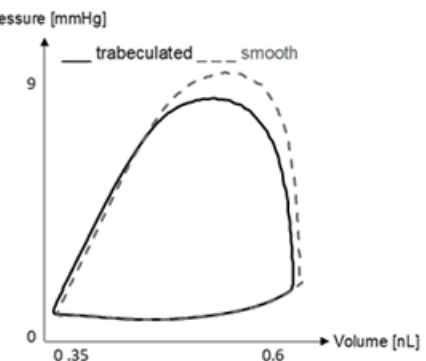
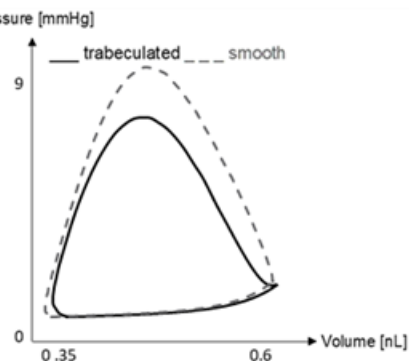
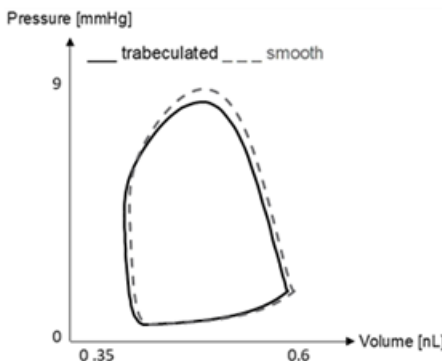
Trabecular Volume Quantification



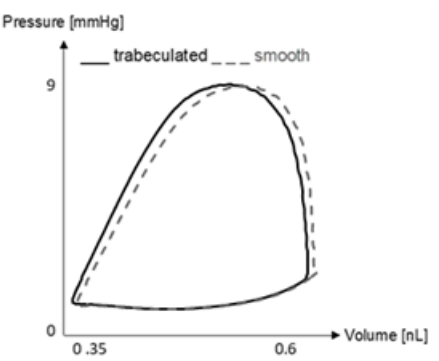
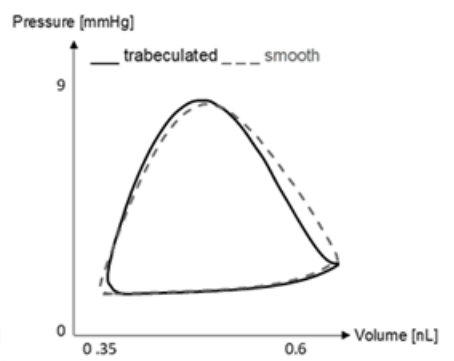
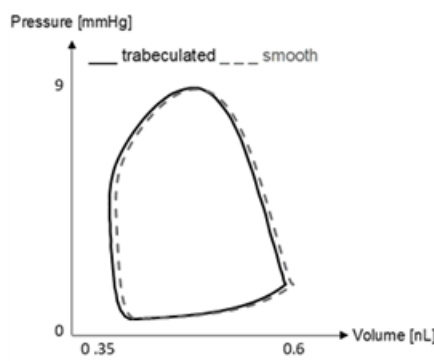
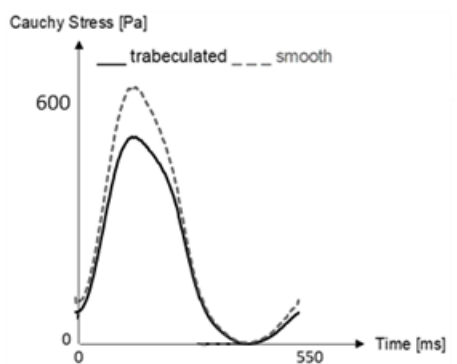
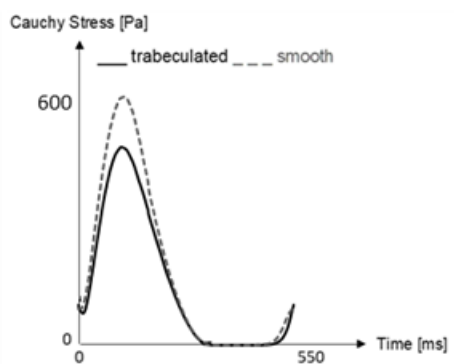
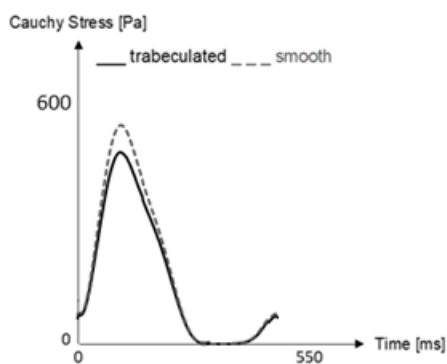








A



B

